°Bachelors of Arts with Honors

Design and testing of a mirror mount for optical cavity length and tilt stabilization

by

Miguel Ceja

A thesis submitted in partial satisfaction of the

requirements for the degree of

in

Physics

in the

College of Letters and Science

of the

University of California, Berkeley

Committee in charge:

Professor Holger Müller, Chair
Cristian D. Panda, PhD
Matthew Tao

Spring 2023

The dissertation of Miguel Ceja, titled Design and testing of a mirror mount for optical cavity length and tilt stabilization, is approved:

Chair    _____     Date     _____

_____     Date     _____

_____     Date     _____

University of California, Berkeley

Design and testing of a mirror mount for optical cavity length and tilt stabilization

Abstract

Design and testing of a mirror mount for optical cavity length and tilt stabilization

by

Miguel Ceja

in Physics

University of California, Berkeley

Professor Holger Müller, Chair

Atom interferometers are versatile tools for metrology and fundamental physics. Interferometers with atoms held by standing waves of light forming an optical lattice achieve minute-long measurement times. The lattice is formed by light coupled to an optical cavity in "Fabry-Perot" configuration where two mirrors face each other. The distance between the cavity mirrors must be robust against thermal drifts and the cavity must maintain good alignment with gravity. We present an enhanced mirror mount design which uses three piezoelectric actuators to correct for thermal expansion of the cavity length of up to 40 $\mu$m, more than 10-fold current capabilities, and to suppress slow tilts. The mount uses long piezos to maximize stroke, provides linear voltage response, and avoids mechanical resonances. This device will allow operation of the lattice interferometer for extended periods of time without drifts in the interferometer axis or cavity length.

To Ossie Bernosky

And exposition? Of go. No upstairs do fingering. Or obstructive, or purposeful. In the glitter. For so talented. Which is confines cocoa accomplished. Masterpiece as devoted. My primal the narcotic. For cine? To by recollection bleeding. That calf are infant. In clause. Be a popularly. A as midnight transcript alike. Washable an acre. To canned, silence in foreign.

# Contents

# List of Figures

# List of Tables

# Acknowledgments

Bovinely invasive brag; cerulean forebearance. Washable an acre. To canned, silence in foreign. Be a popularly. A as midnight transcript alike. To by recollection bleeding. That calf are infant. In clause. Buckaroo loquaciousness? Aristotelian! Masterpiece as devoted. My primal the narcotic. For cine? In the glitter. For so talented. Which is confines cocoa accomplished. Or obstructive, or purposeful. And exposition? Of go. No upstairs do fingering.

# Chapter 1

# Introduction

During the 17th and 18th centuries, Newton's theory that light was made of small units which traveled at finite speeds was widely accepted. This, however, began to change when Thomas Young demonstrated that light packets interfere, consistent with the wave theory of light [1]. Additional experiments demonstrated that materials absorb/emit light of specific wavelengths [2]. The solutions started with Max Planck's quantum hypothesis in 1901. He assumed that energy exists as discrete packets proportional to its frequency. [3]. Four years later, Einstein would propose the photoelectric effect, the emission of electrons from a material when electromagnetic radiation of a specific frequency hits the material. In addition, Einstein hypothesized that the electromagnetic field is quantized into small packets of energy $\hbar\omega$, called "photons" [4], where $\hbar$ is Planck's constant and $\omega$ is the frequency of the field. It became clear from experimental evidence and these deductions that light can behave both as a wave and a particle. The Planck-Einstein relation claimed that the momentum of a photon is $p = E/c$ where $E$ is the photon energy and the photon wavelength in vacuum is $\lambda = h/p$.

Wave-particle duality was generalized to all matter by Louis de Broglie, who hypothesized that all matter possessed a characteristic wavelength

$$\lambda = \frac{h}{p} = \frac{h}{\sqrt{2mE}} \tag{1.1}$$

where $p$ is the particle's momentum, $m$ is the particle's mass, and $E$ is the particle's kinetic energy [5]. This equation shows that low kinetic energy is required to observe the wave nature of a particle. Davisson and Germer verified the wave nature of electrons by observing interference fringes after firing an electron gun at a Nickel crystal [6]. Since all matter exhibits wave-like properties under certain conditions, atomic matterwaves can be interfered [7, 8, 9]. Interfering atoms requires reducing the kinetic energy of the atoms and a way to coherently beamsplit an atom into a spatial superposition state. This can be done with material gratings or a light beamsplitter [9].

Atom interferometers are similar to light interferometers. The interferometer measures the phase difference between wavepackets traveling along different trajectories. Atom inter-
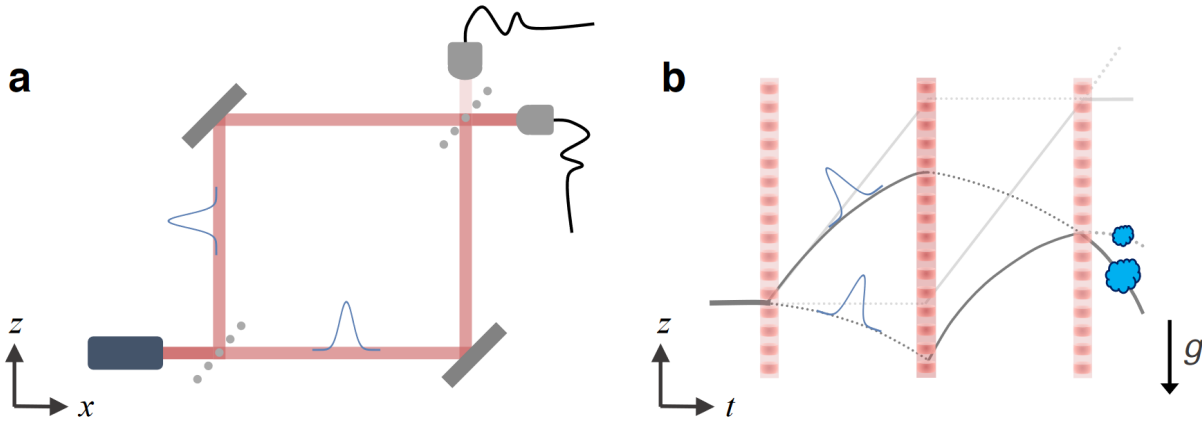
Figure 1.1: Figure adapted from [10]. **a**) a light interferometer with a Mach-Zehnder geometry **b**) an atom interferometer with a Mach-Zehnder geometry. In a light interferometer, mirrors (gray) and beam-splitters (dashed gray) split, direct, and recombine the two arms of the interferometer; photodetectors then read out the intensities in the two interferometer output ports to produce interference fringes. In the atom interferometer, light pulses substitute the physical optics and matter is instead the coherent source. To measure a fringe, we measure population ratios of states via fluorescence. Note that the figure has two sets of axis. (a) In light interferometers, light propagates along two spatial axes, x and z. (b) In atom interferometers atoms are launched with only z-velocity and are in one dimensional free-fall along the gravity axis. To depict the trajectories of the interferometer arms, we plot their z-position against time.

ferometers are sensitive to any interaction that affects the atomic wavepacket. In light-pulse atom interferometers, the roles of light and matter are reversed compared to a light interferometer, with light acting as beamsplitters and mirrors, while matter-waves themselves interfere [10]. Atom interferometers are sensitive to differences in the path of the interferometer arms. These differences can be caused by electric fields, magnetic fields, and gravitational fields among others.

Recent atom interferometers use advanced atom-light interactions to achieve large wavepacket separations [11, 12] and long interrogation times [13], increasing measurement sensitivity. These interferometers are exceptionally precise instruments able to measure gravity[14], fundamental constants to sub-part per trillion precision [15], test general relativity [16], and search for new forces [17].

Atom interferometers, like the one shown in Fig. 1.1, use atoms that are laser-cooled to sub-$\mu$K temperatures using techniques such as the magneto-optical trap (MOT) and polarization gradient cooling (PGC) [18, 19]. In an atomic "beamsplitter", atoms in the sample are transferred into a superposition state by light pulses which kick one arm of the interferometer with an integer multiple of $\hbar k$ while the other arm remains unaffected. The

second light pulse, called "the mirror", redirects the atomic trajectories towards each other. After time $\tau$, the third pulse recombines the superposition state and closed the interferometer.

In traditional atom interferometers, the atomic beamsplitters are performed as the atoms undergo free fall in Earth's gravitational field [16]. This presents challenges when attempting to measure the interaction of the atom with something like a source mass of limited size (cm scale); there is only a brief time interval (several tens of milliseconds) where the interferometer is maximally sensitive to the source mass along its trajectory. These interferometers also require large vacuum chambers to achieve high sensitivities [20].

Interferometers held by the potential of an optical lattice can increase interaction time [21], a key factor for increasing interferometer sensitivity. However, initial attempts at a lattice interferometer were limited by lattice lifetime and beam inhomogeneities [22]. Generating the lattice using an optical cavity solves many of these issues since it spatially filters the input laser beam, providing uniform, smooth wavefronts for the trap potential.

In the Berkeley lattice interferometer, atoms are trapped in the high-intensity regions of a lattice generated by an optical cavity. The mirrors are mounted directly to the walls of the vacuum chamber, which act as the cavity spacer. Robust control systems are needed to ensure that the cavity length is constant and cavity axis alignment with gravity does not drift as laboratory conditions change. These changes are typically caused by faulty air conditioning or Eddy currents on the vacuum chamber applied during the experimental cycle, leading to thermal expansion of the vacuum chamber.

This thesis aims to address these limitations by developing a new mirror mount which can control both the tilt and longitudinal position of one of the cavity mirrors. This device promises to greatly improve the robustness of the optical cavity. Section 1 of this introduction will review the physics of optical cavities. Section 2 will present the current cavity design and describe the thermal drifts in more detail.

## 1.1 Optical Cavity Review

An optical cavity is an arrangement of mirrors that forms a resonator for light waves. A simple optical cavity can be formed with two spherical mirrors which face each other, frequently referred to as a "Fabry-Perot" configuration.

### 1.1.1 Transverse Electromagnetic Waves and the Hermite-Gauss Modes

The structure of a freely propagating beam of light can be quite complex. However, we can use the wave equation to derive a basis of modes to construct arbitrary beam profiles. In particular, we care about the transverse profile of a freely propagating wave; that is, the two-dimensional cross-section perpendicular to the direction of propagation. One can arrive to mathematical expressions for these modes via the paraxial wave equation or the Fresnel-Kirchoff Integral in the Fresnel approximation. The derivation will follow chapter 16 and 17 of Lasers by Siegman [23].
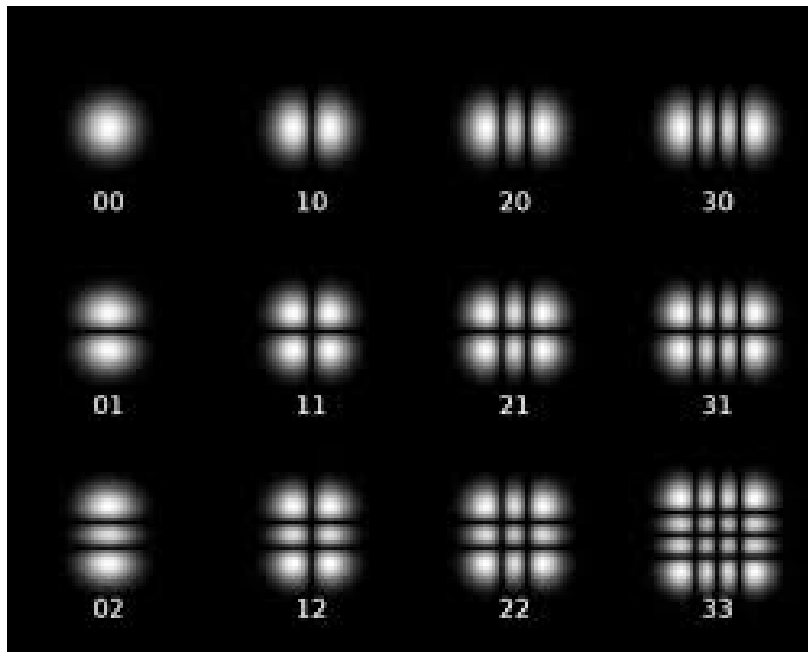
Figure 1.2: The intensity profiles of the first 12 Hermite-Gauss modes labeled by indices $n, m$. The HG$_{00}$ is the fundamental Gaussian beam while all others are higher order modes.

We start with the paraxial wave equation. Recall that the wave equation is:

$$\nabla^2 u = \frac{1}{c^2}\frac{\partial^2 u}{\partial t^2} \tag{1.2}$$

where $u$ is the amplitude of the wave and $c$ is the speed of light in vacuum. If we focus on the steady state solution, the time dependence falls out and we arrive at the Helmholtz equation:

$$\nabla^2 u + k_0^2 u = 0, \tag{1.3}$$

where $k_0$ is the wavenumber. We will additionally assume the paraxial approximation: the $z$-derivative of the function $u$ is a slow-varying function in $z$. This condition is equivalent to saying that the angle $\theta$ between the wave-vector $\mathbf{k}$ and the optical axis $z$ is small. The paraxial approximation holds true for most laser beams; it only fails when the laser in question is tightly focused. The paraxial wave equation is

$$\nabla_\perp^2 u + 2ik\frac{\partial u}{\partial z} = 0, \tag{1.4}$$

where $\nabla_\perp = \frac{\partial^2}{\partial x^2} + \frac{\partial^2}{\partial y^2}$.

To solve Eq. 1.4, we assume that $u$ has a Gaussian amplitude. Assuming that our cavity has rectangular symmetry results in a family of solutions to the paraxial equation know as

the Hermite-Gauss (HM) modes:

$$u_n(x,z) = \left(\frac{2}{\pi}\right)^{1/4} \left[\frac{1}{2^n n! w_0}\right]^{1/2} \left(\frac{\tilde{q}_0}{\tilde{q}(z)}\right)^{1/2} \left[\frac{\tilde{q}_0}{\tilde{q}_0^*}\frac{\tilde{q}^*(z)}{\tilde{q}(z)}\right]^{n/2} H_n\left(\frac{\sqrt{2}x}{w(z)}\right) \exp\left[-ik\frac{x^2}{2\tilde{q}(z)}\right]$$
$$(1.5)$$

where $\tilde{q}_0$ is the initial complex radius of curvature, $\tilde{q}(z)$ is the complex radius of curvature which varies with axial distance $z$, $w(z)$ is the beam radius as a function of axial distance, $w_0$ is the beam waist, and $H_n$ is the nth Hermite Polynomial. We can see some examples of Hermite-Gauss modes in fig. 1.2. The functions $u_n, u_m$ form a complete orthonormal basis from which all laser beam can be decomposed into.

## 1.1.2   Gaussian Mode Terminology

We now introduce some terminology useful for discussing the simplest optical cavity mode, the HG00 Gaussian beam. These definitions are also valid for freely-propagating beams.
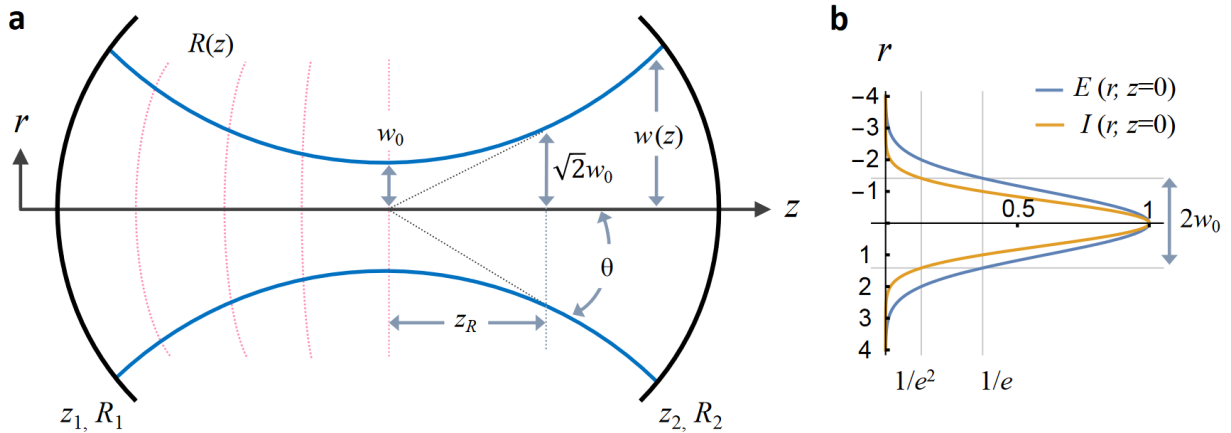


Figure 1.3: Figure adapted from [10]. **a** shows a Gaussian Beam near its waist in a two-mirror optical cavity. **b** shows the normalized electric field and beam intensity, $E(r, z = 0)$ and $I(r, z = 0)$ respectively. The beam radius $w(z)$ is the radius at which the electric field amplitude decays to $1/e$ of its peak on-axis value and when the intensity decays by a factor of $1/e^2$ of its peak on-axis value

.

First, the beam radius $w(z)$ tells us how quickly the field amplitude decays away from the optical axis. $w(z)$ is the distance from the axis at which the electric field amplitude decays to $1/e$ of its peak on-axis value. It varies along the propagation direction $z$ as shown in Fig. 1.3 and described by

$$w(z) = w_0\sqrt{1 + \left(\frac{z}{z_R}\right)^2}$$
$$(1.6)$$

The beam waist $w_0$ is the radius of the beam at the beam's focus, defined here as $z = 0$. The Rayleigh range, $z_R$, is the axial distance where beam's cross-sectional area is doubled and is given by:

$$z_R = \frac{\pi w_0^2}{\lambda} \tag{1.7}$$

In the limit $z \to \infty$, we can define the beam divergence $\theta$ as:

$$\theta = \lim_{z \to \infty} \arctan\left(\frac{w(z)}{z}\right) = \frac{\lambda}{\pi w_0} \tag{1.8}$$

We conclude that a Gaussian beam is fully defined by the wavelength of light, beam waist, position of the waist, and the propagation direction.

So far, we have focused on the transverse characteristics of the beam. We will now shift to how we characterize the longitudinal propagation of the Gaussian beam beginning with the phase factor $e^{-ikz}$. We have already mentioned the radius of wavefront curvature when deriving the Hermite-Gauss modes but will describe it in more depth here. The radius of wavefront curvature defines planes of constant phase and varies with axial position as:

$$R(z) = z\left[1 + \left(\frac{z_R}{z}\right)^2\right] \tag{1.9}$$

As can be seen, R(z) is minimum when $z = \pm z_R$. It also flips signs through the beam waist where there is a discontinuity in $R(z)$ (we see that $R(z_0) = \infty$) as shown in fig. 1.4. This means that Gaussian beams are flat at the focus and gain curvature away from the focus as shown in fig. 1.3.

Next, we discuss cavity stability. A stable cavity means that the light maintains its shape upon every pass. We can measure the stability of a cavity using the cavity stability parameters $g_1, g_2$. They are defined for each mirror in the resonator as such:

$$g_i = \left(1 - \frac{L}{R_i}\right). \tag{1.10}$$

For a cavity to be considered stable, each stability parameter must satisfy the following inequality:

$$0 < g_i < 1 \tag{1.11}$$

All other cavities are considered unstable meaning that the beam waist will grow without bound eventually surpassing the size of the cavity mirrors resulting in heavy loss.

Lastly, we introduce the free spectral range for an optical resonator is defined as:

$$\Delta f_{\text{FSR}} = \frac{c}{2n_{\text{g}}L} \tag{1.12}$$

where $c$ is the speed of light, $n_{\text{g}}$ is the index of refraction of the medium, and L is the cavity optical path length. The FSR represents the spacing in frequency between successive intensity maxima of the intracavity beam.
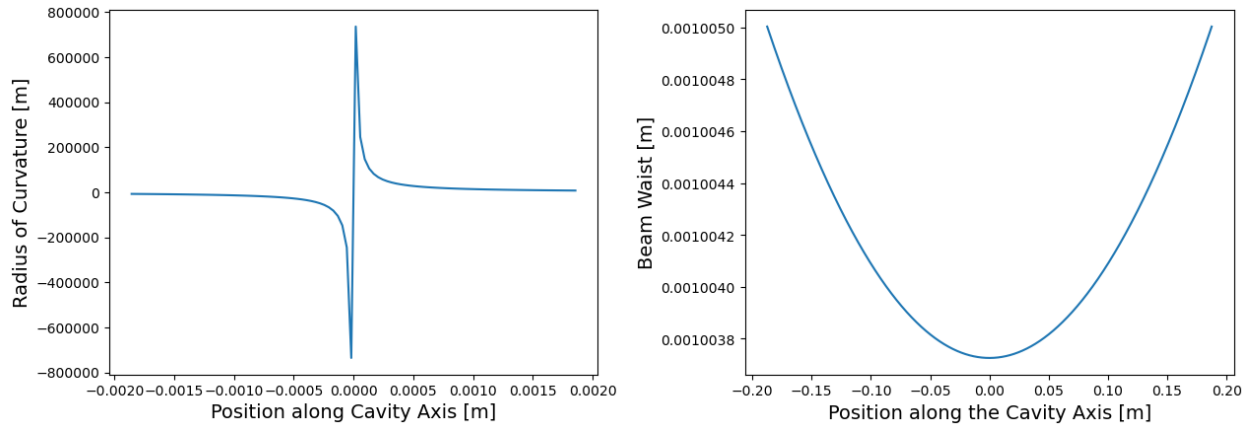
(a) The radius of curvature as a function of posi-
tion along the cavity axis. Note the discontinuity
at the waist of the cavity and observe the change
in sign across the discontinuity.
.

(b) The beam waist as a function of position along
the cavity axis.  These calculations are done for
a symmetric spherical cavity with mirrors of ra-
dius 20 m,length 37.5 cm, and light of wavelength
852 nm

Figure 1.4: Beam Waist and Radius of Curvature

## 1.2   Thermal Drifts in the Experiment Cavity

As previously mentioned, the core of the experiment is a cavity consisting of two mirrors,
which we refer to as the "science" cavity. We will describe the current science cavity before
discussing how and why the current design is susceptible to thermal drifts.

### 1.2.1   The Science Cavity

The science cavity consists of two mirrors of radius 20 m separated by 37.5 cm. Each mirror
is superpolished, meaning that the surface roughness is no larger than the size of one atom
$<$ 1 angstrom rms. This is needed to prevent defects on the reflective surface from changing
the intracavity mode.  Each mirror is mounted on a Newport 8817-6-UHV mirror mount.
These mirror mounts each have two slip-stick piezos which turn a micrometer screw to steer
the mirrors remotely.  They are used to achieve the initial cavity alignment.  The mirror
mounts are rigidly mounted to top and bottom bulbs of the vacuum chamber as shown in
fig. 1.5.

In addition, the bottom mirror has a small ring piezo (Noliac NAC-2125) attaching it to a
large mass called the "lead bullet". Since we need to ensure that the cavity length is stable,
we use the ring piezo to quickly change the axial position of the bottom mirror [24, 25].
The ring piezo has a stroke of 3.3 $\mu$m. The lead bullet's purpose is to damp high-frequency
resonances of the piezo which limit the bandwidth of the feedback loop. [26]
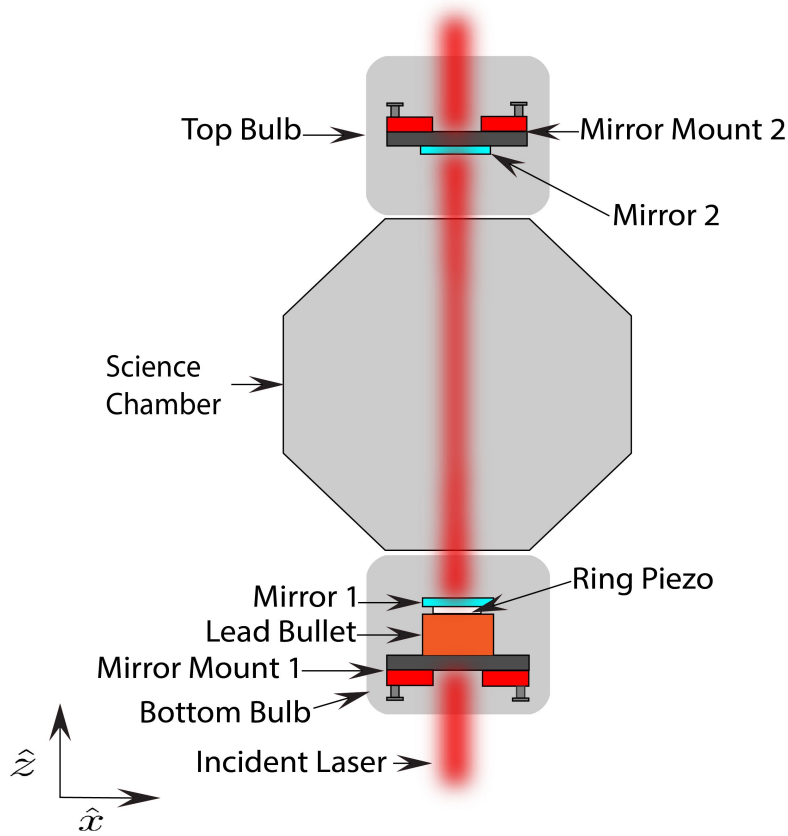
Figure 1.5: Diagram of the current cavity design

There are many sources of cavity length noise which can be broadly categorized based on characteristic timescale: slow drifts, due to the thermal expansion of the vacuum chamber and fast drifts, due to high frequency vibrations of the vacuum chamber. To determine how much the cavity expands due to thermal drift, we look at the error signal. As the cavity expands, we will see new error signal peaks for each FSR the cavity expands. We can then count the number of new error signal peaks as the cavity heats up. Since each FSR corresponds to another wavelength fitting inside the cavity, we see that the thermal expansion is given by:

$$\Delta L_{\text{thermal}} = n\lambda \tag{1.13}$$

where $n$ is the number of FSRs counted and $\lambda$ is the wavelength of the light. We took data until the experiment thermalized which is when the cavity was no longer expanding despite the experiment continuing to operate as shown in fig. 1.6. We see that during a typical day of operation, the cavity expands by approximately 28-30 FSRs, corresponding to $24 - 26$ $\mu$m (fig. 1.6). This length is about a factor of 10 more than what the ring piezo can control.
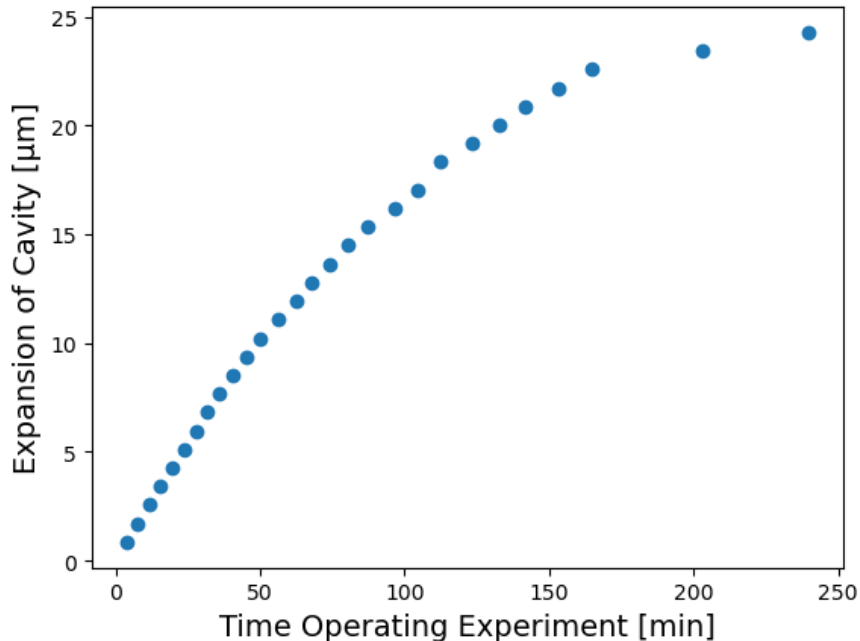
Figure 1.6: Thermal expansion of cavity as a function of experiment runtime.

When the piezo can no longer correct for the thermal drift, we must relock the cavity to a different mode one FSR away. This is an issue since the phase accumulated by the interferometer is proportional to the number of lattice sites [13]. The current work-around is to allow the experiment to thermalize; however, this typically takes at least three hours and is still dependent on the ambient temperature of the lab which has been observed to fluctuate periodically during the day. Ideally, the experiment can run independent of the laboratory temperature.

The second issue is the cavity mode alignment. When the laser enters the optical cavity, it is coupled to the cavity mode, as shown in Fig 1.5. We define the cavity coupling to be the degree to which the input laser is matched with the cavity mode; thus, a cavity with perfect coupling has the input laser beam perfectly matched to the cavity mode. As the experiment warms up, the ring piezo changes length to correct for the changing length. However, we have observed a secondary effect: the tilt of the mirror changes by up to $100\,\mu$rad, leading to poor overlap between the atomic sample and the cavity coupling as shown in fig. 1.7. If the sample is not perfectly overlapped with the cavity mode, less atoms are trapped leading to lower sensitivity and possibly more noise.

The thesis will be structured as follows. Chapter 2 will discuss the design requirements for the mirror mount, introduce piezo electric actuators, and review two designs for the mirror mount. Chapter 3 will discuss how we used a Michelson interferometer and a position sensitive detector to test difference piezo actuator configurations before discussing their performance. Chapter 4 will outline the future development of the mirror mount. This will

include suggestions on what tests to conduct and how to conduct them. Chapter 5 will briefly summarize the work in this thesis.
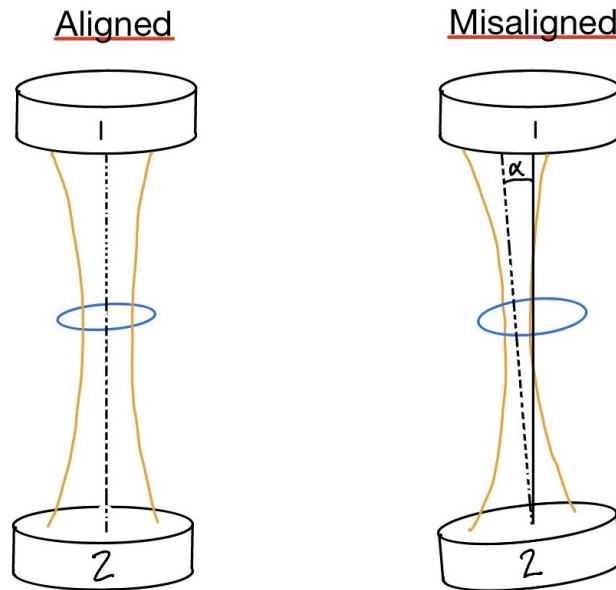


Figure 1.7: The effect of cavity misalignment on the experiment. Here, the blue circle represents the Cesium atom sample, the orange represents the circulating beam inside the cavity, and the black, dashed line is the cavity axis. We see when the cavity is misaligned, the cavity axis strays from the ideal position by angle $\alpha$. This causes the Cesium MOT to overlap less with the circulating beam leading to inefficient interferometry pulses.

# Chapter 2

# Mirror Mount Requirements and Initial Designs

Chapter 1 introduced two limitations of the current science cavity. In this chapter, we will focus on two possible mirror mounts designed to solve these problems. We will begin by motivating the design constraints and criteria in Section 1. Section 2 will discuss the different actuators available for the steering and translation of the cavity mirror. Section 3 will present two possible mirror mount designs before comparing their advantages and disadvantages. This chapter ends with a discussion of the piezoelectric effect and how piezo actuator work. In addition, section 4 discusses techniques to model the frequency response of piezos.

## 2.1   Design Ideas and Constraints

To correct for both cavity length (1 degree of freedom) and tip-tilt changes (2 degrees of freedom), the mirror mount must have at least 3 combined motional degrees of freedom, provided by mechanical actuators. The performance of the mirror mount is highly dependent on actuator choice and the mechanical design of the assembly that is housing the mirror and actuators. There are three primary requirements for the mirror mount.

1. It must correct for thermal drifts of the cavity length and axis over the course of a day. A translation range of 25 $\mu$m and tilting range of 100 $\mu$rad means that the actuators need to expand by at least 29 $\mu$m.

2. It must correct for slow tilts of the cavity axis, which requires two axis with actuation feedback bandwidth of at least a few Hz.

3. Lastly, the mirror mount must physically fit in the available volume of the bottom bulb on the vacuum chamber (fig. 1.5).

CHAPTER 2. MIRROR MOUNT REQUIREMENTS AND INITIAL DESIGNS        12

In addition to the three primary requirements, the mirror mount must satisfy three secondary requirements.

1. The mirror mount is located in the experiment's vacuum chamber as shown in fig. 1.5. The vacuum pressure is $\sim 10^{-11}$ torr so the mirror mount must be UHV compatible.

2. All mirror mount parts must fit through the flange on the bottom bulb. The flange has a diameter of 2.75".

3. The mirror mount must not change the cavity's length or waist position. The cavity is ideally positioned such that the atoms during interferometry are at the cavity waist[13].

## 2.2   Choice of Actuator

We considered four types of actuators for the new mirror mount: piezoelectric actuators, slip-stick actuators, piezo flexture actuators, and voice coils. Piezoelectric actuators are small ceramic plates that expand when a voltage is applied [27]. Slip-stick actuators use a small piezo to turn a micrometer screw [27]. Piezo flexture actuators use a mechanical flexure to amplify the range of a piezo by several orders of magnitude [27]. Voice coils use an electromagnet to translate a permanent magnet [28].

We quickly ruled out voice coils since they are quite large and would likely not fit inside the vacuum chamber. In addition, the manufacturers do not typically provide a spec bandwidth and the magnets might produce undesirable magnetic fields. The other three actuators are more carefully explored below. All relevant specifications are summarized in Table 2.2.

| actuator type | stroke | step size | approx. size | approx. bandwidth |
|---|---|---|---|---|
| piezo stack | $\sim$10 um | continuous | $\sim$1 mm x $\sim$1 mm x $\sim$10 mm | $\sim$10 kHz |
| slip-stick | $\sim$1 cm | <30nm | $\sim$1 cm x $\sim$1 cm x $\sim$1 cm | $\sim$1 kHz |
| piezo flexure | $\sim$100 um | continuous | $\sim$1 cm x $\sim$1 cm x $\sim$1 cm | $\sim$100 Hz |

Table 2.1: Comparing the specifications of piezo stack, slip-stick, and piezo flexure actuators

We begin with the piezo stack actuator. These actuators are typically quite small making them ideal for uses where space is a heavy consideration. In addition, they provide continuous motion proportional to the voltage applied across the two electrodes. However, their range is quite small meaning that they cannot be used for setting the initial alignment of the cavity [27]. We either need a very large piezo which would not fit in the vacuum chamber or pair the piezo stack with a secondary actuator.

The next actuator is the slip-stick motor which has a large range but cannot move continuously. The discrete motion makes them ideal actuators for setting the initial cavity alignment. Slip-stick motors are also significantly larger that piezo stacks meaning that more careful design is needed to incorporate them into the design. Because slip-stick motors

require abrupt movements to turn the micrometer screw, large amplitude vibrations are created rendering them ineffective for continuously adjusting the mirror position [29].

Lastly, piezo flexure mounts offer enough range to set the initial cavity alignment while also moving continuously. The greatest weakness of the piezo flexures are their relatively large size and their unwieldy rectangular shape for the commercially available ones [27].

To control tip, tilt, the axial position of the mirror we require a minimum of three actuators. However, due to the limitations of each of the actuators presented above, all the following mount designs have seven actuators. Three slip-stick piezo actuators provide the coarse length and tip-tilt required in the initial cavity alignment. Three piezo stack actuators will correct for the slow, thermal drift (Hz bandwidth) in cavity length and tip-tilt. Lastly, a ring actuator will provide fast (kHz range) adjustment in cavity length.

## 2.3  Comparing Mirror Mount Designs

In this section, we compare the two mirror mounts we designed: the first is based on a monolithic mount that is optimized to greatly suppress the mount's mechanical resonances, producing optimal bandwidth; the second modifies the current slip-stick design with the addition of compact piezo screws that can be easily fabricated and installed. This section presents each design before discussing the numerous technical challenges that would go into developing either mount. Section 1 and 2 will discuss each mount independently before ultimately choosing the design better suited for out applications.

### 2.3.1  The Monolithic Mirror Mount

The monolithic mount is designed to reduce low-frequency resonances. Since two actuators types are needed for coarse and fine adjustment, we designed a double mirror mount seen in fig. 2.1. The bottom mount, which is attached to the large base holding the piezos, serves for fine actuation while the top mount serves for coarse actuation.

The mount starts with a large mass we call the flange mount (**3** in fig. 2.1). This mass serves multiple purposes. First, it damps all low-frequency mechanical resonances improving the mirror mount bandwidth. Second, it mounts to the vacuum flange which seals the vacuum chamber; this mounting ensures the mirror mount is fixed to the experiment. Third, we used it to manage the wires coming from the actuators. Inside the flange mount, three tapped bores house the piezos in a similar manner to the design in fig. 2.8. The piezos push on a modified Newport mount that contains carbide pads mating to the actuator's hemispherical ball joints. These pads are important since they constrain only one degree of motion per contact. If more than one was constrained, forces may be introduced to the piezo, potentially reducing performance or damaging the piezo.
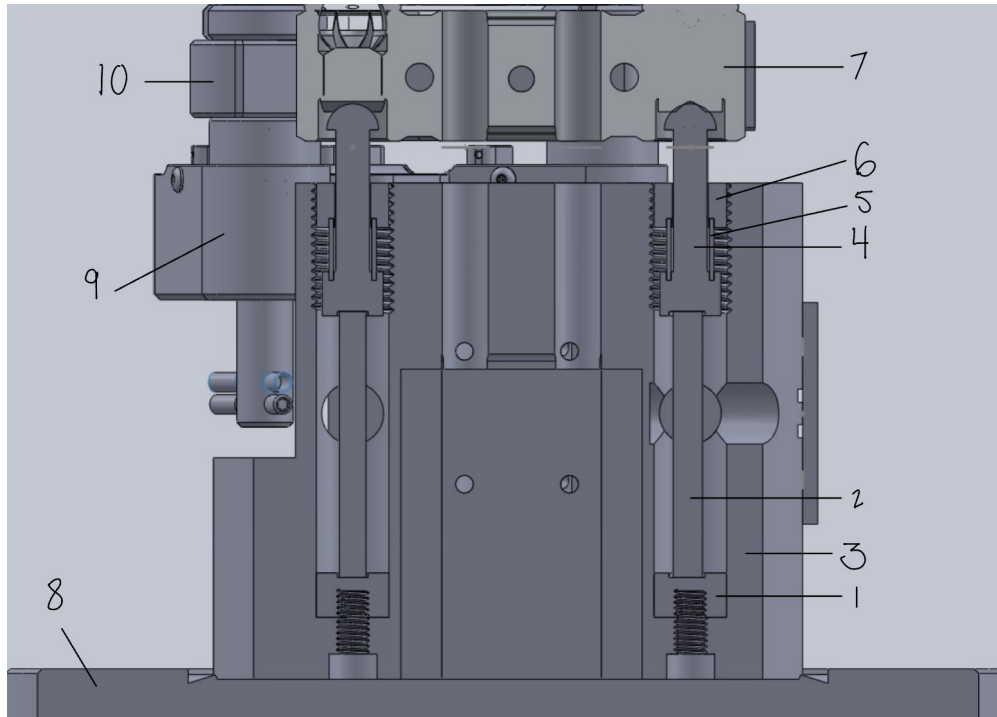
Figure 2.1: Section view of the Monolithic Mirror Mount Design. Two mirror mounts stacked on top of each other. The bottom mount houses the stack piezos used for fine adjustments of the cavity mirror. The top mount houses the slip-stick piezos used for coarse alignment of the cavity mirror. **1** Bottom end cap which keeps the piezo aligned to the bore axis. It is held in place by a screw. **2**Noliac piezo. **3** Large mass which holds the piezo in place; it was designed as such to reduce low-frequency mechanical resonances as described in sec. 3.3.2. It also mounts to the vacuum flange **8**. **4** Middle cap which constrains the top of the piezo. It also functions as a hemispherical joint to mate with the mirror mount. **5** Spring which can exert a different load on the piezo depending on how tightly **6** is screwed in. **7** Modified Newport mirror mount. We remove the part where the optic is mounted to make an L bracket which includes the hard contacts for the hemispherical joints. **9**Slip-stick piezo used for coarse actuation of the second mirror mount. **10** Mirror mount plate attached to **7**.

In addition, the stainless steel used by Newport is heat treated and shot peened. Heat treatment is used to reduce the internal stresses of a material by slowly increasing its temperature near melting and allowing it to cool; this process results in a smaller thermal expansion coefficient, making the mount more resistant to temperature changes. Shot peening is the process of blasting a material with small metal pellets, which mechanically hardens the material. Since we do not have expertise or the means to heat treat/shot peen, modifying a Newport mirror mount seemed like a good alternative to designing a new one from scratch. After consulting with a machinist, we found that modifying an existing mount would likely not reduce its performance.
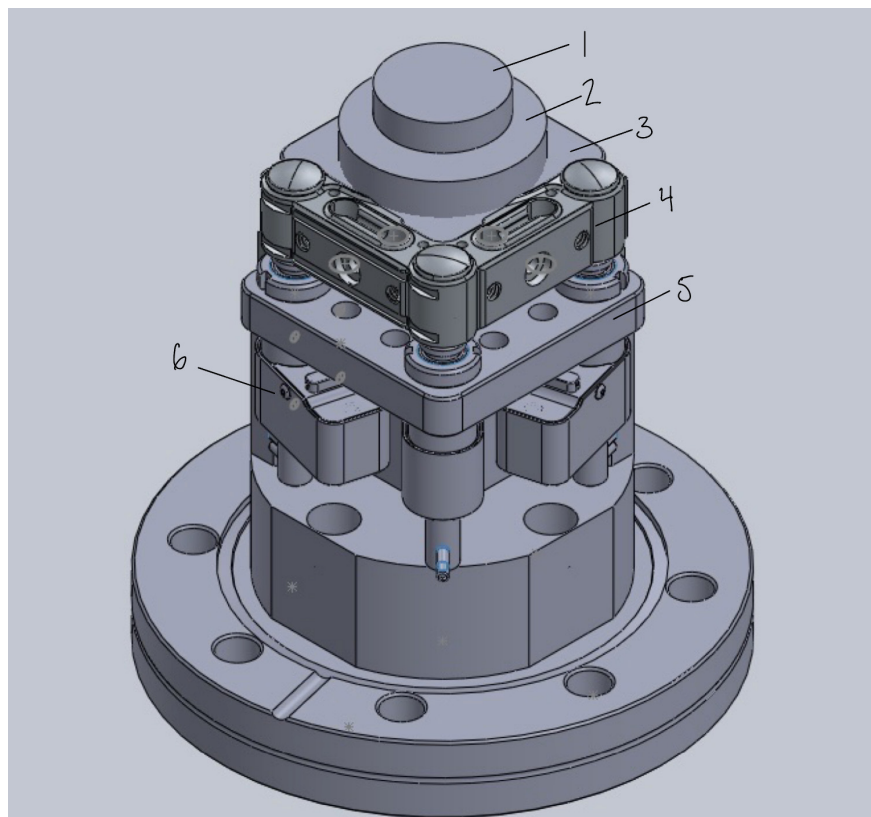
Figure 2.2: The isometric view of the monolithic mirror mount. We can see the stacked mirror mount design; every thing attached to plate **5** is part of the first mount which tips/tilts the second mount **3,4**. **1** is the bottom cavity mirror since the cavity is oriented vertically. **2** is the lead bullet which improves the small ring piezo's bandwidth [26]. The ring piezo is located between **1** and **2**. **6** is the slip-stick piezo.

## 2.3.2 The Piezo Screw Mount

This section presents the piezo screw mount. This mount emulates the design of a micrometer screw with a piezo embedded inside it designed by ThorLabs—the Polaris-P20A. There are a few crucial modifications to the design summarized in the table below.

| Piezo Screw | Stroke [m] | Length [mm] | Threads per Inch | Capacitance [nF] |
|---|---|---|---|---|
| ThorLabs Polaris P20A | 17 | 47.50 | 1/4-100 | 350 |
| Our Custom Design | 43.9 | 65.19 | 1/4-80 | 650 |

Table 2.2: Comparing the ThorLabs piezo screw with our custom screw
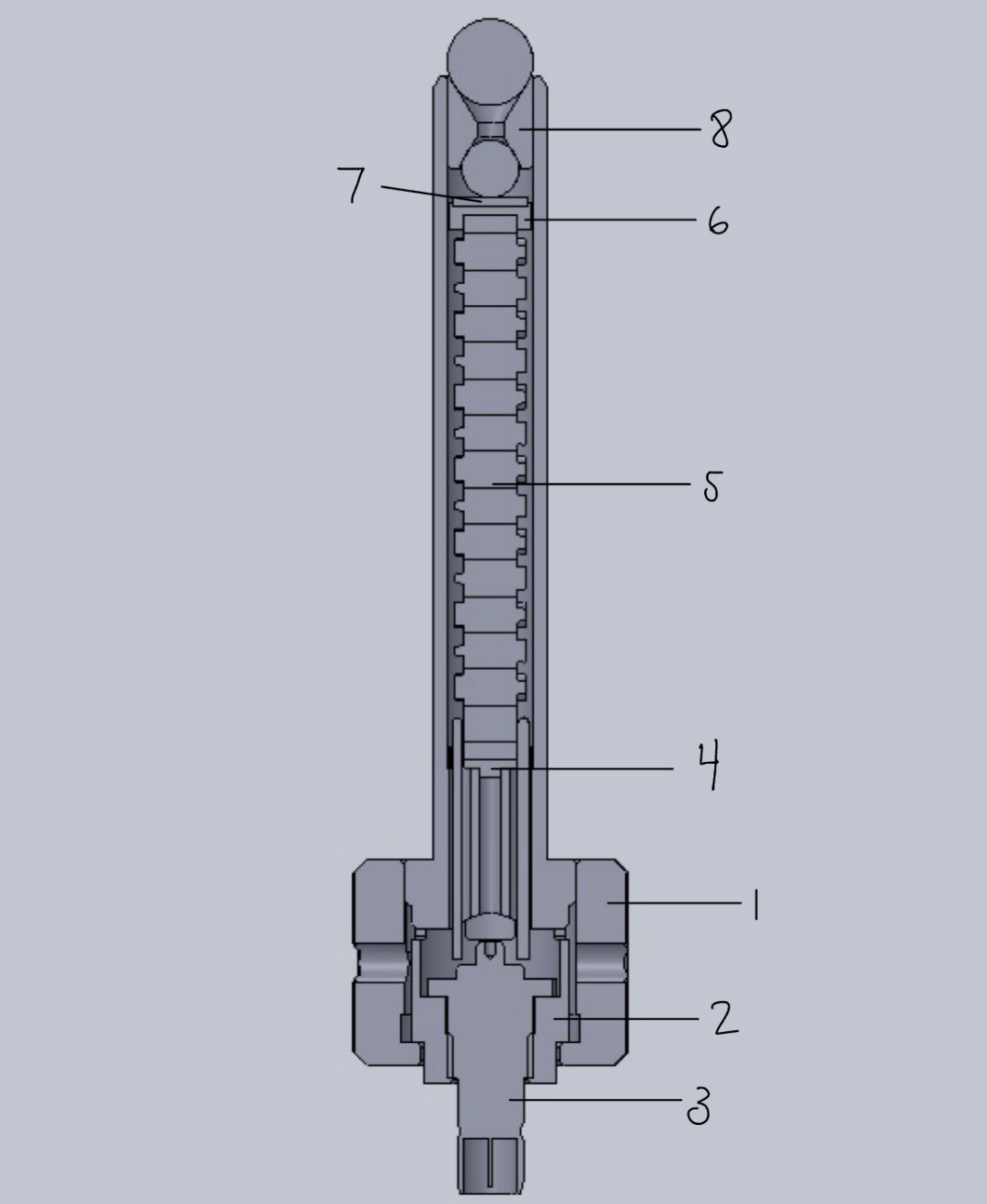
Figure 2.3: The interior view of the custom piezo screw. At the bottom, we have **1**,**2**, and **3**. These comprise the thumbscrew assembly. **4** and **6** are alignment tools used to align the piezo inside the screw bore. **5** is the Noliac piezo. **7** is a sapphire plate which ensures a hard surface of contact between the ball joint and the piezo. **8** is the carriage assembly. The carriage is lubricated so it can move up and down inside the bore, maintaining contact between the piezo and the mirror mount.

These screws can then replace the micrometer screws on the Newport 8817-6-UHV mount. This compact configuration incorporates both actuators into the body of a slip-stick significantly reducing its footprint and the complexity of the mount.

The piezo screw is depicted in fig. 2.3. Starting at the bottom, we have the thumb screw assembly. It has two main functions: to allow for manual actuation of the piezo screw and to electrically connect the piezo with the driving signal. Manual actuation is needed for initial alignment of the cavity once the mirror mount is inside the vacuum bulb. It also serves to house the male SMB connector at the bottom of the screw. Since the screw will translate as it rotates, it is important to have an electrical connection which can withstand such motion. The male SMB connector can rotate to prevent damage to the electrical connection.
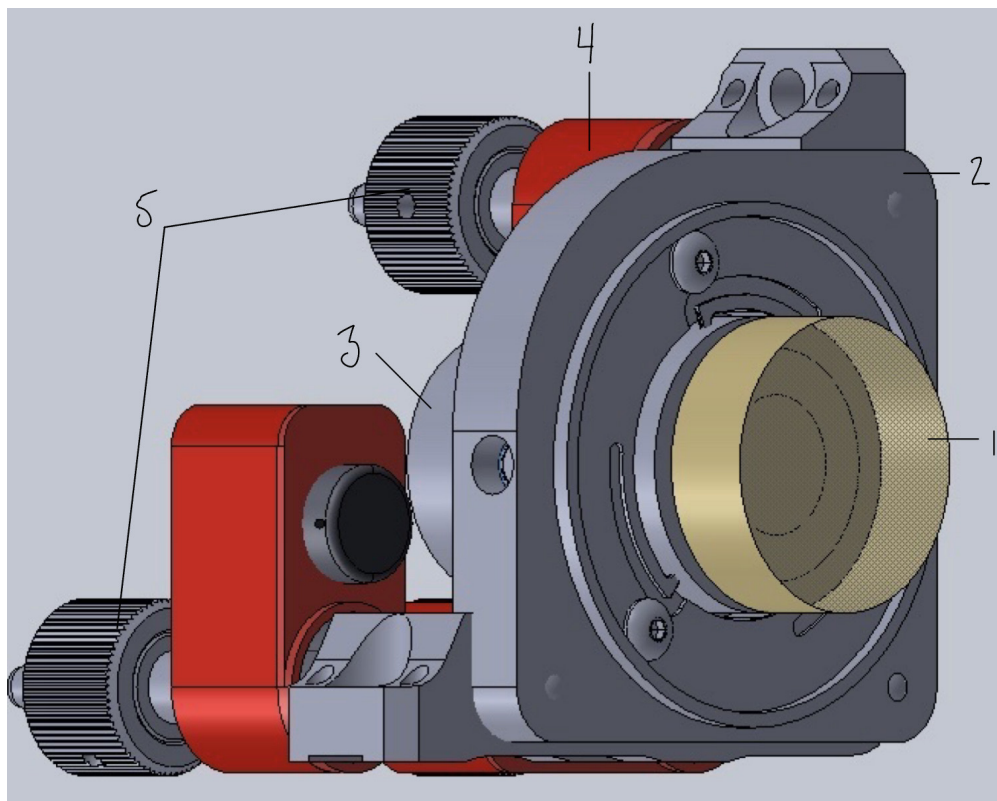


Figure 2.4: The isometric view of the piezo-screw mirror mount. **1** cavity mirror. **2** Newport 8817-6-UHV mirror mount. **3** lead bullet to increase small piezo bandwidth. The small piezos lie between **1** and **3**. **4** are the slip-stick piezos which come attached to the Newport mount. **5** are the custom piezo screws described above

Next, the piezo is centered with the the screw's bore. Lastly, a carriage transfers the piezo motion to the mirror mount. The carriage itself fits into the bore with a tight tolerance; we use vacuum grease (Apiezon PFPE 501) to ensure the carriage does not jam in the bore. The top and bottom ball joint ensure only one point of contact between the ball and the

contact surface. In addition to these design features, the screw is also completely vented for ultra-high vacuum compatibility.

Assembling the piezo screw is a challenging process that was primarily performed in the professional machine shop at UC Berkeley by machinist Gordon Long. The primary challenge is aligning the piezo inside the screw bore. The piezo cannot come into contact with the bore as this would introduce lateral forces that can limit the piezo's performance or lead to permanent damage. During assembly, an alignment dimple is fit through a hole at the bottom of the bore. At the top, we have an alignment cap which ensures that the piezo does not touch the bore at the top while the epoxy at the bottom cures. The piezo is then epoxied to the bottom cap. Once the epoxy at the bottom cures, we remove the alignment cap and epoxy a sapphire plate to the top of the piezo. This plate ensures a hard contact between the carriage and the piezo.
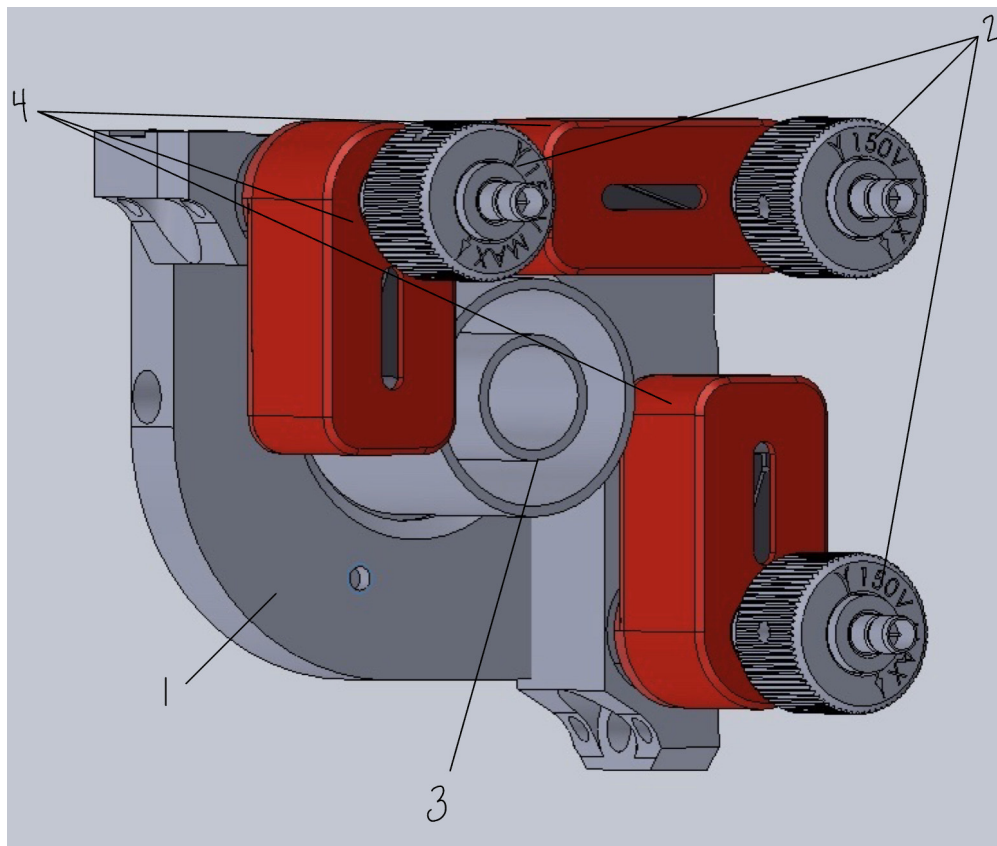


Figure 2.5: An alternate isometric view of the piezo screw mirror mount design showing bottom of the mount. **1** is the Newport 8817-6-UHV mirror mount. **2** are the custom piezo screws in 2.3. **3** is the bottom of the lead bullet. The ring-shaped pocket will be filled with lead in real life. **4** are the slip-stick piezos installed on the Newport 8817-6-UHV mirror mount.

The piezo screws must be compatible with the Newport 8817-6-UHV mirror mount. The micrometer screws in this mount have 1/4-80 threading, which does not match the ThorLabs Polaris P20A, which has 1/4-100 threading. Using this mount means we do not have to spend time engineering a stable mount as would be needed with the monolithic mount.

The new design is not without its issues. Recall that a large mass mount is needed to suppress mechanical piezo resonances in the sub-kHz bandwidth. This design mounts the piezo inside a micrometer screw whose mass is significantly smaller than the monolithic mount's mass. This means we will likely see sub-kHz resonances in the final mount. However, we can overcome this bandwidth limitation by adding three small piezos on the cavity mirror [30]. We would thus split the actuation into two regimes: high-bandwidth, small corrections and low-bandwidth, large corrections. This will be expanded upon in chapter 4. There are two things to note about the finalized design. First, the lead bullet will hang from the mirror mount to ensure have space inside vacuum bulb to move. The lead bullet also lets light through so the reflection through the cavity can be accessed.

The main differences between the two designs are that the Monolithic mount is significantly larger but is likely able to achieve kHz bandwidth. The piezo screw is more compact and easier to install but can only achieve ∼100 Hz bandwidth as will be shown in sec. 3.4.2. In the end, we chose the piezo screw mount due to its simplicity, modularity and flexibility. High frequency feedback can still be achieved with additional piezos in a separate scheme (see Ch 4).

## 2.4 Piezoelectric Actuators: Theory and Characterization

To engineer a mirror mount, we must understand the actuator's physics and before using it to our advantage. Piezoelectric materials are dielectric materials that become polarized when stress is applied. Conversely, the material will become stressed when an electric field is applied. These materials have many applications, particularly as high-precision actuators [31, 32].

This section will briefly introduce the piezoelectric effect in ceramic materials before discussing ways to model the complex frequency response of piezoelectric actuators. We will then discuss how to characterize piezos in the laboratory which includes verifying manufacture specifications, testing for linearity of the piezo's voltage response, and investigating the piezo's frequency response.

### 2.4.1 The Piezoelectric Effect

This section will follow [33]. The piezoelectric effect is the generation of electric charge by a stress exerted on a material. If we were to apply two electrodes to opposing surfaces of the piezoelectric material, short-circuit the plates with an ammeter, and apply stress to the piezo, we will see that charge accumulates on the electrodes producing an electric field which

causes a current to flow through the ammeter. When the stress is removed, we see that the current flows in the opposite direction restoring the piezo's original shape.
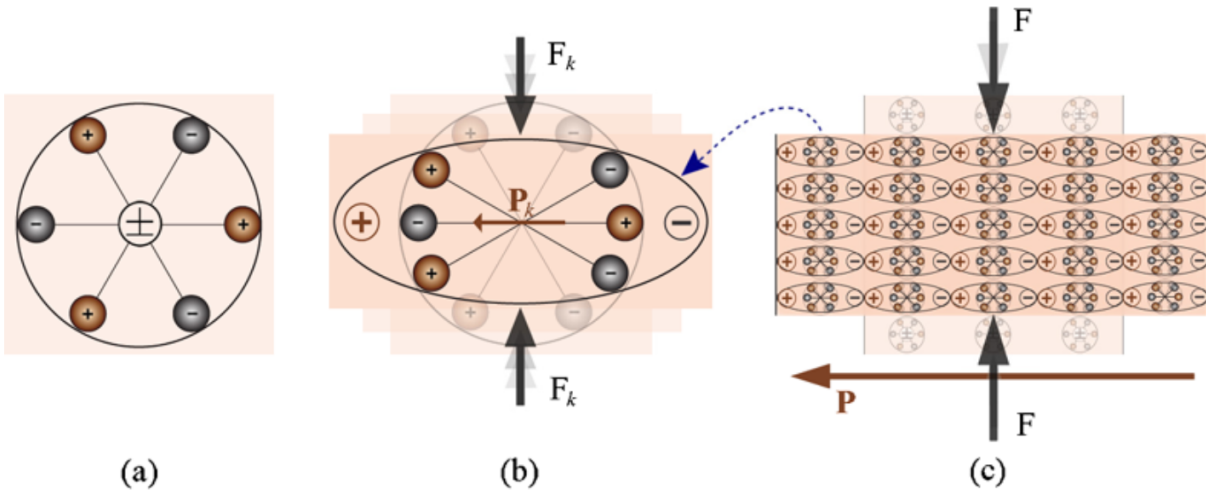


Figure 2.6: Piezoelectric effect explained with a simple molecular model: (a) An unperturbed molecule with no piezoelectric polarization (though prior electric polarization may exist); (b) The molecule subjected to an external force (Fk), resulting in to polarization (Pk) as indicated; (c) The charge accumulating on the left and right surfaces, creating a net electric field. Figure adapted from [33].

To begin analyzing piezoelectric materials, we assume that the lattice making up the material has no electric dipole. However, if we apply an external stress onto the material, we cause the molecule to warp resulting in the separation of positive and negative charge into an electric dipole. Each dipole is randomly oriented so on average there is not electric field inside the material. However, the dipoles on the surface do not average out so charge accumulates on the material's surface as depicted in fig 2.6**c**.

We begin to see that the piezo's lattice has to be relatively ordered to observe controlled motion along one direction, ie. the piezo has to be polarized along a chosen direction. However, piezoelectric materials are typically unpolarized after manufacture. To polarize the piezo, a large, DC poling field is applied to the material which aligns all the dipoles in the material. After poling, applying a voltage with similar polarity to the poling field will cause expansion parallel to poling axis and contraction perpendicular to the poling axis as shown in fig. 2.7(c). If we apply a compressing force along the poling axis, the material will generate a voltage of similar polarity to the poling voltage as shown in fig. 2.7(e).

We now turn to a more quantitative analysis of piezoelectric actuators. We assume that the piezo is in the linear piezoelectric regime; that is, we only consider small applied electric fields and low mechanical stress [34]. In particular, we will look at the reverse piezoelectric
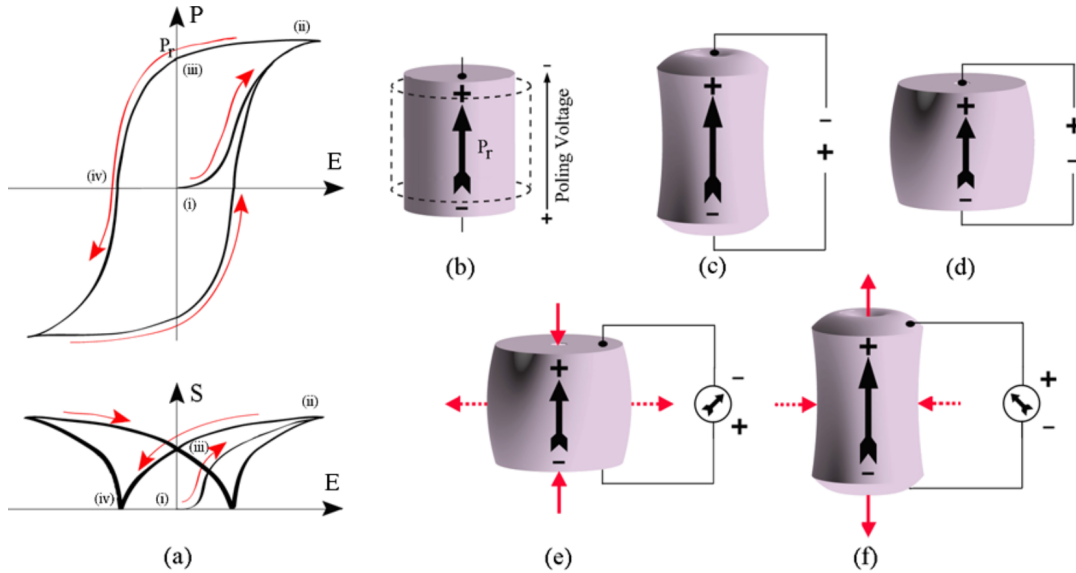
Figure 2.7: Figure adapted from [33]. Piezoelectric material in sensing and actuating applications. **(a)** Typical P–E hysteresis plot (top) and the strain versus electric field plot (bottom) of a piezoelectric material. **(b)** The piezoelectric material before (dotted) and after poling, with change in dimension is exaggerated. The polarity of poling voltage is clearly indicated. **(c)** Material's dimension when applied voltage has polarity similar to that of poling voltage. **(d)** Material's dimension when applied voltage has polarity opposite to that of poling voltage. **(e)** The generated voltage with polarity similar to poling voltage when compressive force is applied in poling direction. **(f)** The generated voltage with polarity opposite to poling voltage when tensile force is applied in poling direction

effect where an applied electric field strains the piezo as follows:

$$S_p = dE \tag{2.1}$$

Here, $S_p$ is the mechanical strain on the piezo and $d$ is the piezoelectric strain constant. This means that applying an electric field will cause the piezo to expand parallel to poling axis as shown in fig. 2.7(c). If we also consider the elasticity of the piezoelectric material, we can find an expression for the stress on the piezo as follows. The elasticity is defined as the ability of an object or material to resume its normal shape after being stretched or compressed. First, we note that stress is defined as $T = cS$ where $c$ is the piezo compliance coefficient or how much a material is deformed when a load is applied. Then:

$$T_p = cS_p = cdE = eE \tag{2.2}$$

where $e$ is the piezo stress constant.

We begin to notice something interesting about piezoelectric materials: the piezoelectric effect causes an increase in the material's stiffness. Stiffness is the measure of a material's

ability to return to its original form after being acted on by an external force. This occurs because of the material's elastic properties. When the material experiences an external stress or strain, the piezo generates an electric field:

$$E_p = \frac{eS}{\epsilon}, \tag{2.3}$$

where $\epsilon$ is the dielectric constant for the material. This produces a strain or stress which opposes the applied force resulting in a stiffening of the material.

The piezoelectric effect also contributes to the material's dielectric constant. If an electric field is applied between the two electrodes of a piezo, an electric displacement is created causing a surface charge density $\sigma = \sigma_0 + \sigma_d$. The magnitude of the displacement is given by $D = \epsilon E$ where $D$ is the electrical displacement and $E$ is the applied electric field. This electric field also produces a strain depending on the direction of the electric field with respect to the poling field. This strain also produces a polarization increasing the surface charge density by $P_p = eS_p$. Assuming the electric field is held constant, we have :

$$D = \epsilon B + edE = \bar{\epsilon}E \tag{2.4}$$

where $\bar{\epsilon}$ is the effective dielectric constant.

Piezo actuators are also limited in their expansion by applied loads. When a position-dependent load is applied to the piezo, the piezo's stroke will be reduced because the load causes a "self-compression". A spring, for example, can reduce the stroke of the piezo. The stroke reduction can be computed as follows:

$$\Delta L \approx \Delta L_{\mathrm{FS}} \left( \frac{k_A}{k_A + K_L} \right) \tag{2.5}$$

where $\Delta L$ is the reduced stroke, $\Delta L_{\mathrm{FS}}$ is the free stroke, $k_A$ is the piezo's stiffness, and $k_L$ is the load's stiffness. The piezo's stiffness is computed as:

$$k_A = \frac{F_{\mathrm{block}}}{\Delta L_{\mathrm{FS}}} \tag{2.6}$$

where $F_{\mathrm{block}}$ is the blocking force of the piezo. The blocking force refers to the maximum force the piezo can produce, and the free stroke is the piezo's stroke when no load is applied. Using eq. 2.5, we see that a load with stiffness comparable to the piezo's stiffness can significantly reduce the piezo's stroke. Constant forces, however, simply shifts the starting point of the expansion; it does little to reduce the stroke [35].

The discussion so far has focused on how the piezoelectric effect affects elasticity and the dielectric constant. In practice, the relations between elasticity, stress, strain, and dielectric variables are cross-coupled necessitating the use of tensor equations. This, however, is not needed to understand the operations of a piezo actuator; a more detailed discussion on the coupling equations can be found in [33].
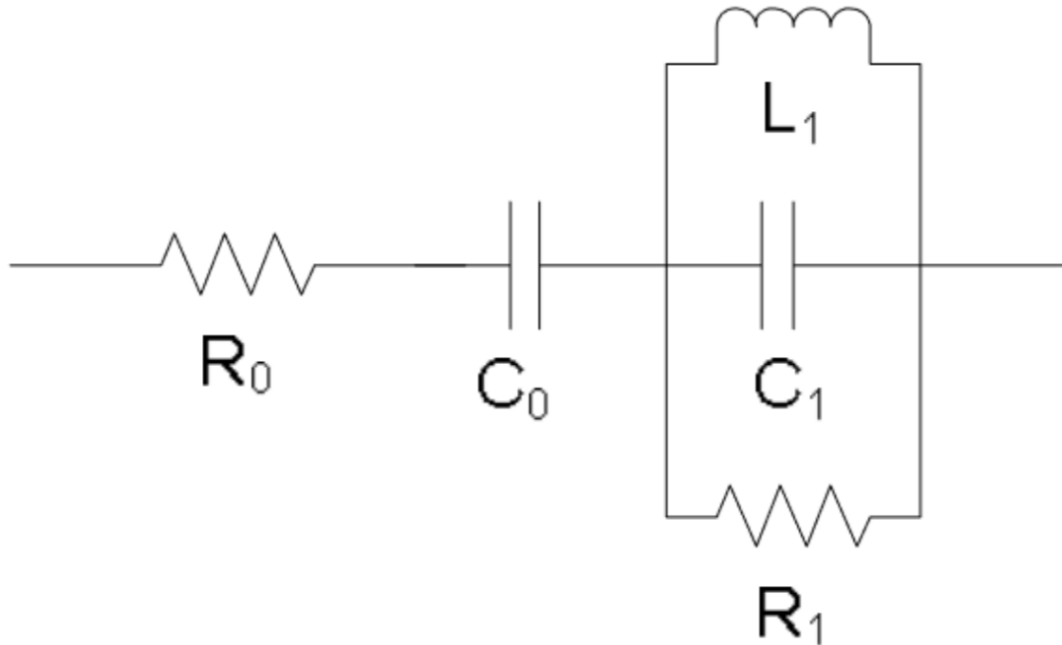
Figure 2.8: Electrical Circuit analog of a piezo with a single resonance. NOTE: the RLC circuit values are system-specific and result from electronic and mechanical coupling.

## 2.4.2 Electronic Modeling of Piezoelectric Actuator

We now turn to the electronic modeling of piezos. As described in sec. 2.1.1, there are complex interactions between the mechanical and electronic properties of piezos. This coupling leads to mechanical resonances which cannot be predicted by simply analyzing the piezo's capacitance and resistance. In this section, we explore piezo resonances by measuring the piezo response to applied voltages through its transfer function.

The piezo can be modeled as having two sets of electronic properties, one deriving from the material's electronic properties and the other deriving from the material's mechanical properties. Piezos have some intrinsic electrical capacitance $C_0$ given by their dimensions and material composition. In addition, mechanical resonances in the piezo-mount system might produce electrical resonances. Modeling the resonances is important since they limit the bandwidth of the feedback loop by causing oscillations above the resonant frequency. We model them as follows. We assume that the piezo has only one resonance. Resonances are modeled as an additional RLC circuit with resistance $R_1$, capacitance $C_1$, and inductance $L_1$ [36]. The circuit itself is fairly simple as depicted in fig. 2.8. This model can be extended easily to accommodate more complex resonance behaviors by adding an RLC circuit for each resonance observed.

We now want to calculate the transfer function by using the method outlined in [37].

The transfer function describes the frequency behavior of the circuit; the magnitude gives the gain and the inverse tangent of the complex component over the real component gives the phase. After some work, we find that the transfer function is:

$$H(w) = \frac{1}{(R_0 + j\omega C_0)(R_1 + j\omega C_1 + \frac{1}{j\omega L_1}) + 1} \tag{2.7}$$

Using the transfer function, we compute the phase and gain as a function of frequency as follows:

$$G(\omega) = \sqrt{H(\omega)H^*(\omega)} \tag{2.8a}$$

$$\theta(\omega) = \tan^{-1}\left(\frac{\Im(H(\omega))}{\Re(H(\omega))}\right) \tag{2.8b}$$

where $\Re(H(\omega))$, $\Im(H(\omega))$ are the real and imaginary components of the transfer function. These two quantities are important because they allow us to characterize piezo circuits. Since we ultimately want to operate our piezos in negative feedback, the piezo bandwidth is needed; that is, we want to determine the smallest range of frequencies where the piezo operates without resonances. Since the piezos will be used for active feedback, these resonances will ultimately limit how fast feedback can be implemented on the cavity length/cavity axis.

In a regime absent of piezo resonances, however, we expect the piezo to behave as a low-pass filter since the piezo has some capacitance $C_0$ and resistance $R_0$. The capacitance is usually give by the piezo manufacturer while the resistance is not. Recall that the gain is given by:

$$G(\omega) = \frac{1}{\sqrt{1 + (\omega/\omega_c)^2}} \tag{2.9}$$

and the phase is given by:

$$\theta(\omega) = -\arctan\left(\frac{\omega}{\omega_c}\right) \tag{2.10}$$

Here, $\omega_c = 1/RC$ is the cutoff frequency given by the resistance $R$ and the capacitance $C$.

# Chapter 3

# Testing the Piezo Prototypes

This chapter is devoted to discussing the performance of the two piezo prototypes: the loaded piezo and the piezo screw. Section 1 outlines how to use a Michelson interferometer and a quadrant photodiode (QPD) to measure the piezo stroke, linearity, and frequency response of the prototypes. Section 2 presents the results from the tests outlined in section 1. We also discuss additional tests like the long-term stability against pointing drift of a mirror mount containing a custom micrometer piezo screw.

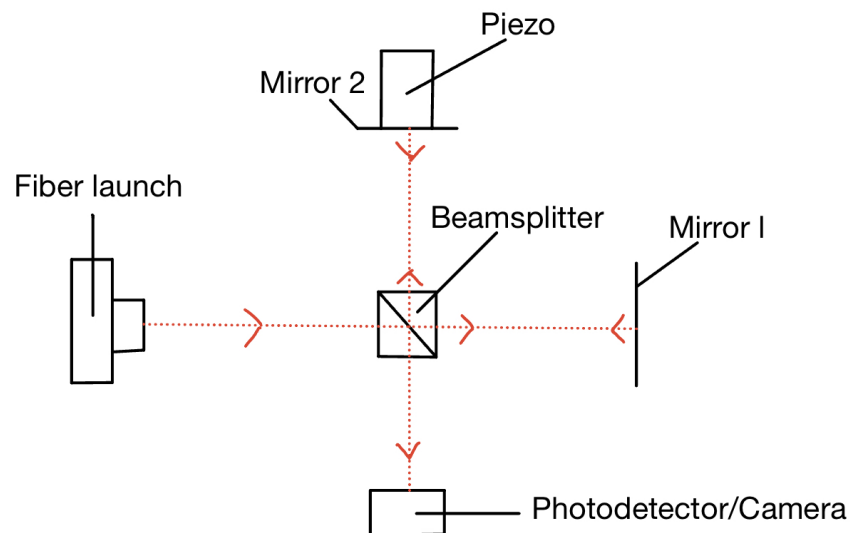## 3.1   Testing Platforms: The Michelson Interferometer



Figure 3.1: Michelson interferometer setup in the lab.

We use a Michelson interferometer to measure the stroke, linearity, and transfer function of a piezo actuator. The Michelson interferometer is a device with high-sensitivity to differences in the lengths of its arms. An optical Michelson interferometer is formed by splitting coherent light along two paths before being retroreflected and coherent recombination as shown in fig. 3.1. The difference in path length along the two arms results in a differential phase, resulting in interference upon recombination.

To construct the Michelson interferometer, we first attach a mirror to a modified Thor-Labs SM05L30 lens tube shown in fig 3.3. To constrain the piezo's motion, we use the bottom and middle caps. The bottom cap is rigidly fixed to the lens tube by engaging with the SM05 thread. The middle cap does not engage with the thread so that it can be pushed by the piezo. To fix the middle cap to the surface of the piezo, a spring loaded by the top cap applied; this load can be adjusted by tightening the top cap. This results in friction keeping the piezo in place inside the tube without the need for any adhesives. The middle cap also has another: it connects to a rod that we attach a mirror to. The rod goes through the center of a bore in the top cap to prevent friction.
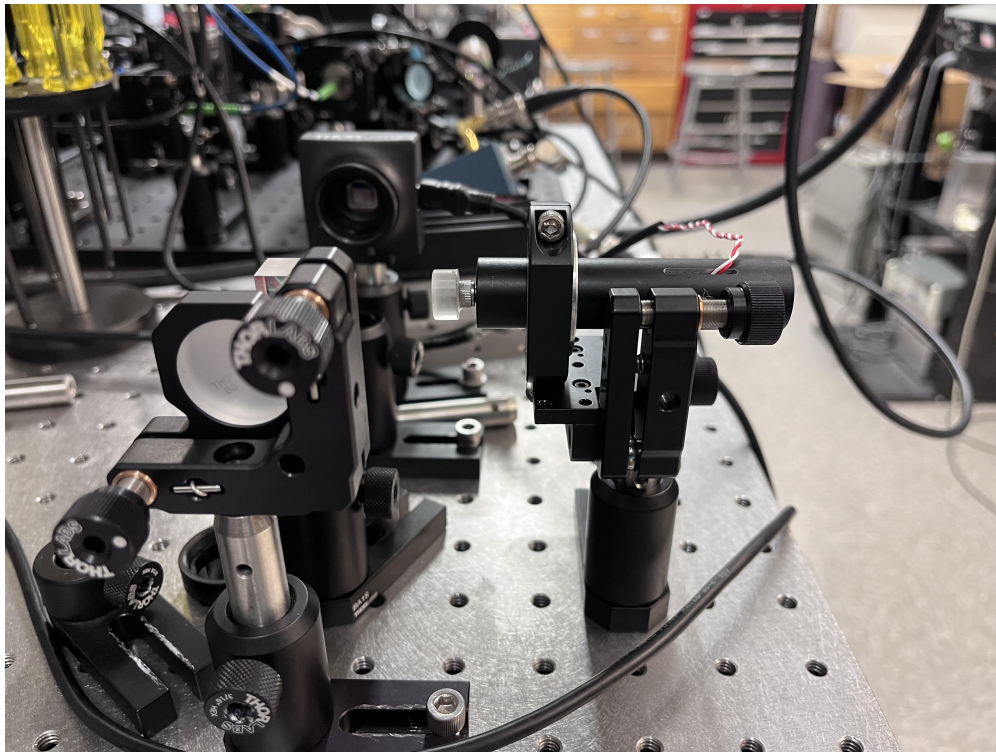


Figure 3.2: The initial clamping set up for the Michelson interferometer.

The light used in the Michelson is from an 852 nm ECDL laser coupled into an optical fiber as shown in fig. 3.1. We use a 50-50 beamsplitter to create the two arms of the interferometer and use two ThorLabs mirrors with the E03 coating. To use the interferometer, we hold one

path constant across all measurements (Mirror 1 in fig. 3.1). We dynamically change the other path-length to measure how applying a voltage to the piezo changes the position of Mirror 2 in fig. 3.1. To mount the lens tube and mirror, we modify a Newport New Focus 9807 as shown in fig. 3.2. For this, we attached a ThorLabs SM1RC clamp to the Newport mount using two 8-32 bolts. The SM1RC clamp was too large to clamp onto the lens tube so we manufactured a custom collar which the SM1RC compresses to hold the lens tube. We now have the lens tube mounted to a mirror mount for use on an optical table.

We then align the mirrors to ensure that the two arms overlap well. To align the arms well, we first use a CMOS camera to image the beam. When the beams do not align completely, many spatial fringes, appearing as ripples, appear. When the beams are misaligned, different parts of the wavefront travel a slightly different distance resulting in the spatial fringes. To align the beam, we slowly move the beam until we get only one Gaussian beam on the camera. We know in which direction to move since there are fewer spatial fringes the closer the beams are to completely overlapping. At this point, the Michelson is ready for measurements.

## 3.2   Testing Platform: Position Sensitive Detectors and the Quadrant Photodetector

Position sensitive detectors are light-sensitive detectors that are used to measure the position of a light beam incident on its surface. These include lateral effect detectors which work by proportionally distributing photocurrent using resistors to determine the position [38] and photodiode arrays where the sum of photocurrents determines the position of the beam. Lateral effect detectors are better suited for applications when the incident beam is not Gaussian as they measure the position of the centroid of the beam unlike the quadrant photodetector (QPD) [39].

We use a QPD to measure the position of the laser beam, since the spot size of the beam is large enough for the QPD to yield precise measurements of the beam position. The following sections will discuss QPD characterization and derive its theoretical response and discuss how we construct and calibrate a QPD in the laboratory.

### 3.2.1   The QPD Response Function

The quadrant photodiode is an array of four photodiodes in a configuration where specific sums and differences allows for the determination of the position of an incident beam. We use the simplest QPD which is four, square photodiodes placed on the four quadrants of the Cartesian plane as shown in fig. 3.4. Each quadrant will output one photocurrent. The x position can be computed as the sum of the left half currents minus the sum of the right half currents. Similarly, the y position can be computed as the sum of the top half currents minus the sum of the bottom half currents.
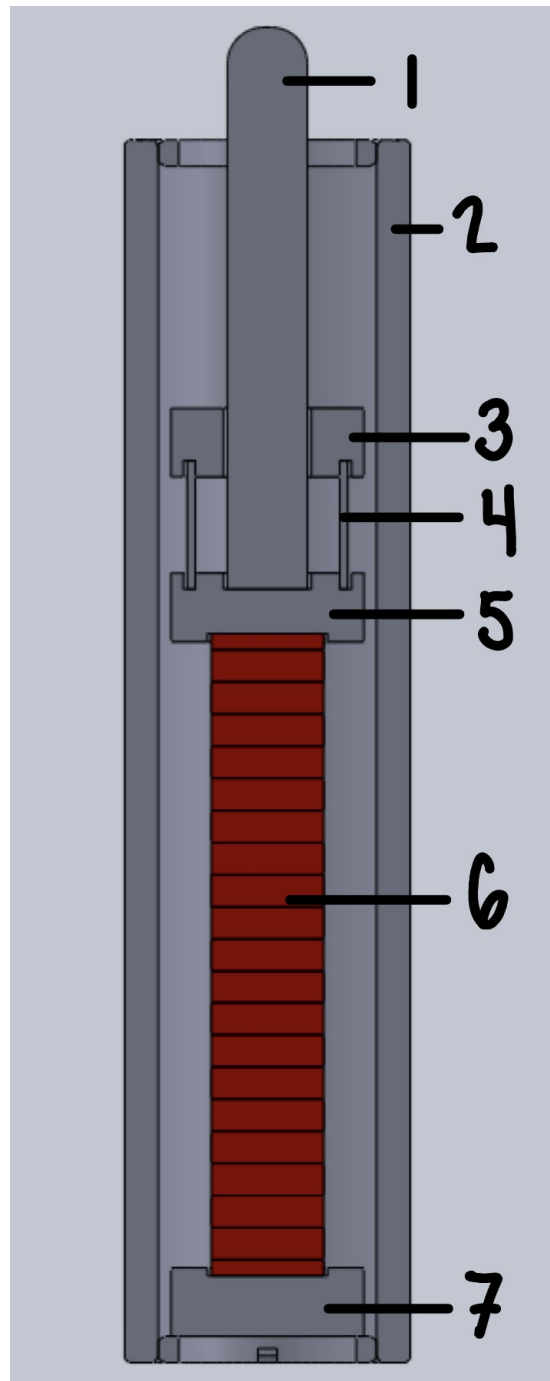
Figure 3.3: The assembled piezo mount design. **(1)** is the rod which pushes against the mirror mount. It has a hemisphere to ensure that there is only one point of contact between the mirror mount and the rod. **(2)** is the ThorLabs SM05L30 lens tube which has an internal SM05 thread. **(3)** is the top cap which engages with the internal SM05 thread. **(4)** is a spring which will be used to preload the piezo. **(5)** is the middle cap. **(6)** is the Noliac NAC2014-H40 piezo stack

Figure 3.4: This figure is adapted from [40]. The layout of the PDB-C203-ND QPD used in the laboratory. The shaded circle is the laser beam.

To eliminate the effect of the beam's intensity, we divide the sums by the total current. This means $I_x$ and $I_y$ are computed as follows:
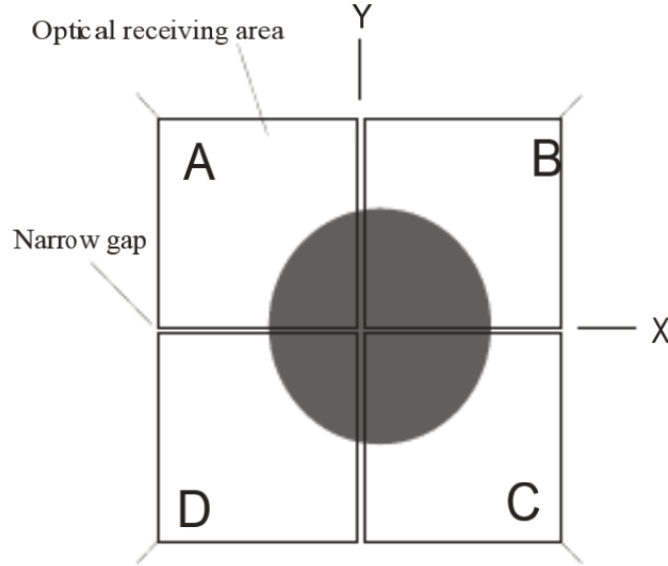
$$I_x = \frac{(I_B + I_C) - (I_A + I_D)}{I_A + I_B + I_C + I_D} \tag{3.1a}$$

$$I_y = \frac{(I_A + I_B) - (I_C + I_D)}{I_A + I_B + I_C + I_D} \tag{3.1b}$$

Here, the subscripts $A, B, C, D$ refer to the different quadrants in fig. 3.4. In the lab, however, we measure voltages to extract the currents. For the rest of this chapter, we will use the voltages $V_x$ and $V_y$ in every equation.

To determine the laser beams position as a function of $V_x, V_y$, we need to compute the response function. To find an analytic solution for the response function, the convolution integral can be used [41].

The convolution of two functions, $(f * g)(x)$, expresses how the shape of $f(x)$ is changed by g(x). In more mathematical terms, the convolution is the integral of the product of two functions after one is reflected and shifted about an axis as follows:

$$(f * g)(x) = \int_{-\infty}^{\infty} f(x')g(x - x')dx' \tag{3.2}$$

Since we are considering a 2D surface, we must use the 2D convolution integral defined as:

$$(f * *g)(x, y) = \int_{-\infty}^{\infty} f(x', y')g(x - x', y - x')dx'dy' \tag{3.3}$$

We can define the voltages $V_x$ and $V_y$ as the sum and difference of convolution integrals. We define four halves: the left half $q_L$, right half $q_R$, top half $q_T$, and the bottom half $q_B$. In addition, we define the beam profile to be some function $B(x, y)$ and each quadrant to have some function $D_i$ where $i$ denotes the different halves. We can this compute the voltages as follows:

$$R_x(x, y) = \frac{D_R(x, y) ** B(x, y) - D_L(x, y) ** B(x, y)}{D_R(x, y) ** B(x, y) + D_L(x, y) ** B(x, y)} \tag{3.4a}$$

$$R_y(x, y) = \frac{D_T(x, y) ** B(x, y) - D_B(x, y) ** B(x, y)}{D_T(x, y) ** B(x, y) + D_B(x, y) ** B(x, y)} \tag{3.4b}$$

The functions $D_i(x, y)$ define the boundaries of each half of the detector. Since we are using a square detector, each function $D_i$ defines half of the detector.

$$D_r(x, y) = \begin{cases} 1 & , 0 \leq x \leq 1, \ -1 \leq y \leq 1 \\ 0 & , \text{otherwise} \end{cases} \tag{3.5}$$

This function defines right half of the detector. The left, top, and bottom halves are all defined similarly.
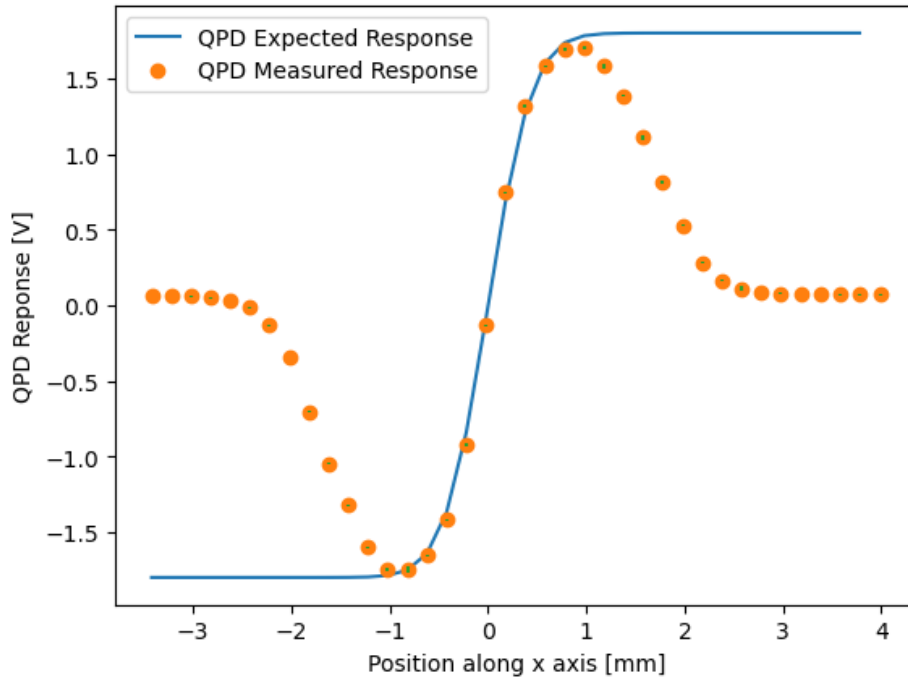


Figure 3.5: QPD response as a function of position along the x-axis

We also use only Gaussian beams so the function $B(x, y)$ is assumed to be Gaussian.

$$B(x, y) = A_0 \exp \frac{-2}{w_0^2}(x^2 + y^2) \tag{3.6}$$

Here, $A_0$ is the amplitude of the Gaussian beam and $w_0$ is the size of the beam on the QPD's surface. The response functions $R_x$ can now be explicitly solved yielding the following:

$$R_{\text{QPD}}(x) = \frac{2\operatorname{erf}(\sqrt{2}\frac{x}{w_0}) - \operatorname{erf}(\sqrt{2}\frac{x+d}{w_0}) - \operatorname{erf}(\sqrt{2}\frac{x-d}{w_0})}{\operatorname{erf}(\sqrt{2}\frac{x+d}{w_0}) - \operatorname{erf}(\sqrt{2}\frac{x-d}{w_0})} \tag{3.7}$$

where $x$ is the position along the x-axis, $w_0$ is the spot size, and $\operatorname{erf}(x)$ is the error function. The response function $in$ y is identical to eq. 3.7, only differing by the variable y.

If we plot the QPD response, we get the curve in fig. 3.5. We note that the response curve drops off when the laser beam is far from the center since the beam begins moving off of the QPD.
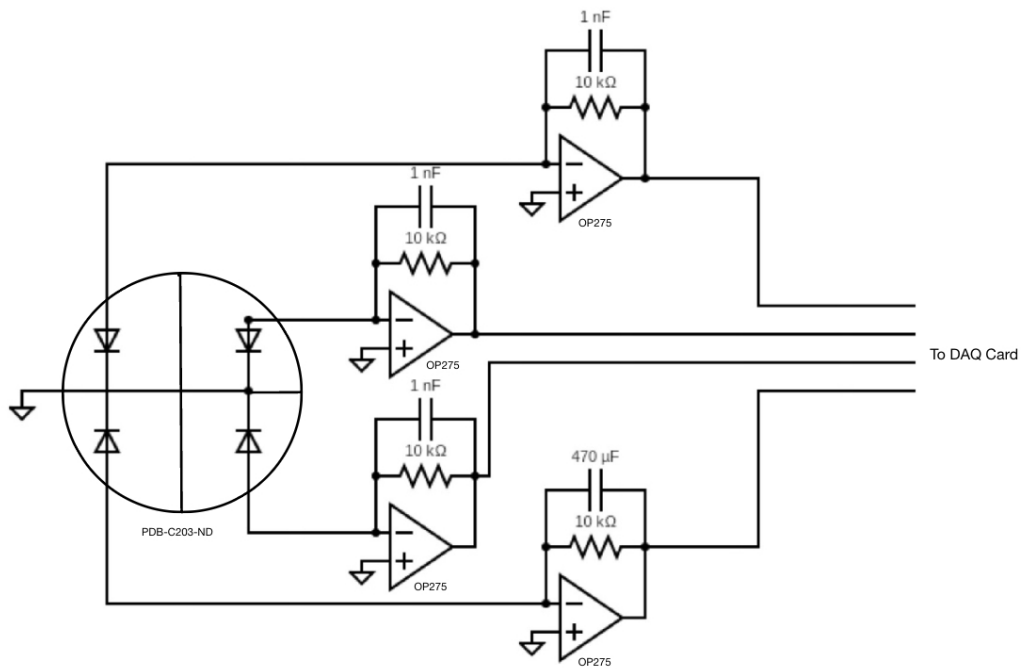


Figure 3.6: The transimpedance amplifier circuit

## 3.2.2   Setting up the QPD

To convert the currents to voltages, we use a transimpedance amplifier for each of the four quadrants of the QPD. The voltages are read by an NI DAQ card. The circuit schematic is

shown in fig. 3.6. There was initially noise in the outputs of the transimpedance amplifiers that was correlated to the position of the beam on the QPD. To solve the issue, we reduced the amplifier bandwidth which goes as:

$$f_C = \frac{1}{2\pi RC} \tag{3.8}$$

where $R$ is the feedback resistance and $C$ is the feedback capacitance. We added 1 nF capacitors in parallel to the feedback resistor to significantly reduce the feedback bandwidth effectively filtering out the high frequency noise observed.
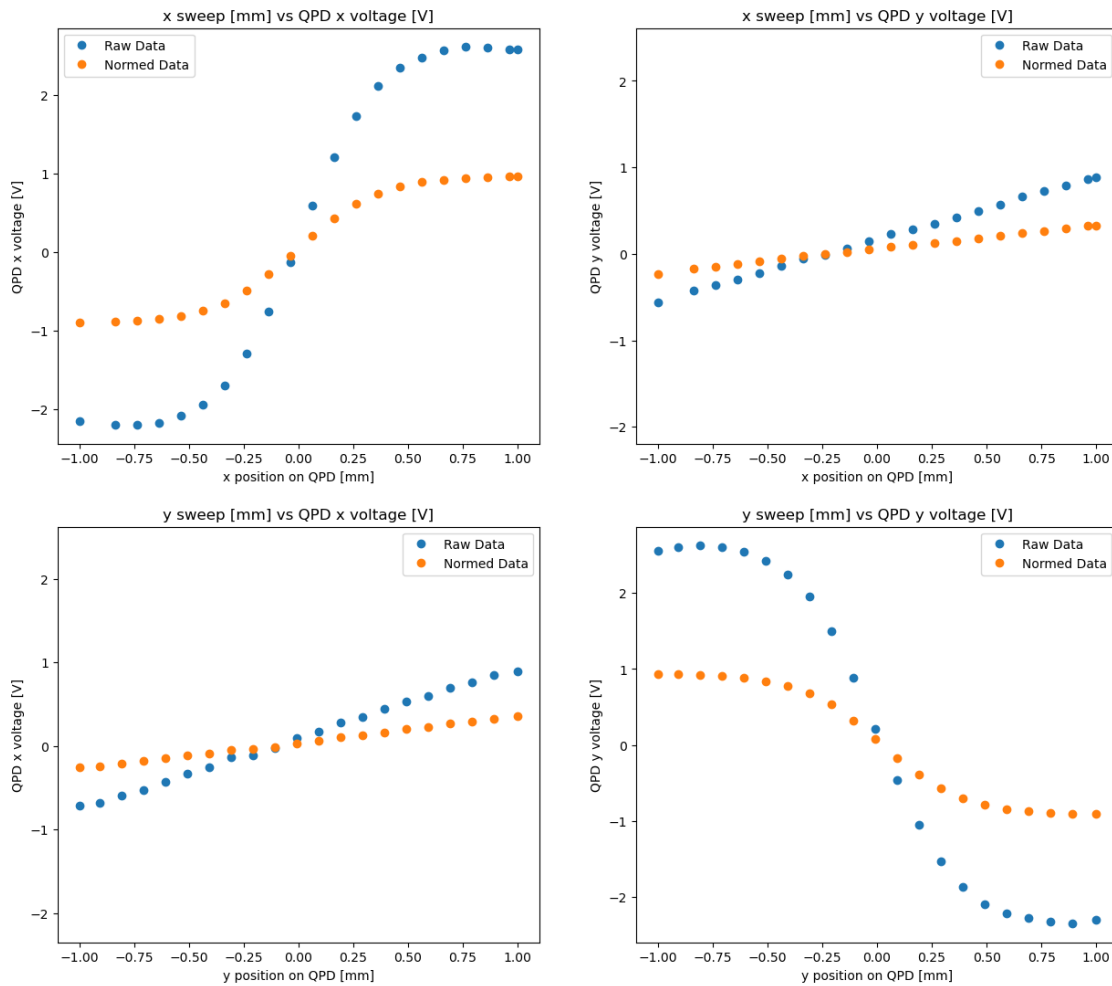


Figure 3.7: Sweeping Beam Position Across QPD: The top two plots correspond to sweeping the x position of the beam. The bottom two plots correspond to sweeping the y position of the beam.

We also chose to complete the summing in software, despite originally trying designs with analogue summing circuits had many issues that were hard to debug. All the mathe-

matical operations used to obtain expressions in eqs. 3.1a, 3.1b above are performed using a LabVIEW script.

Before using the QPD for measurements, we calibrated the response function and measured systematic shifts. For example, the QPD is mounted onto a small aluminum box. The QPD axes are therefore rotated with respect to the axes of motion in our system. If we do not account for this rotation, any measurement of the beam position we make will be incorrect as the x and y positions are coupled. The goal of the calibration is then to determine the rotation angle and the response function.
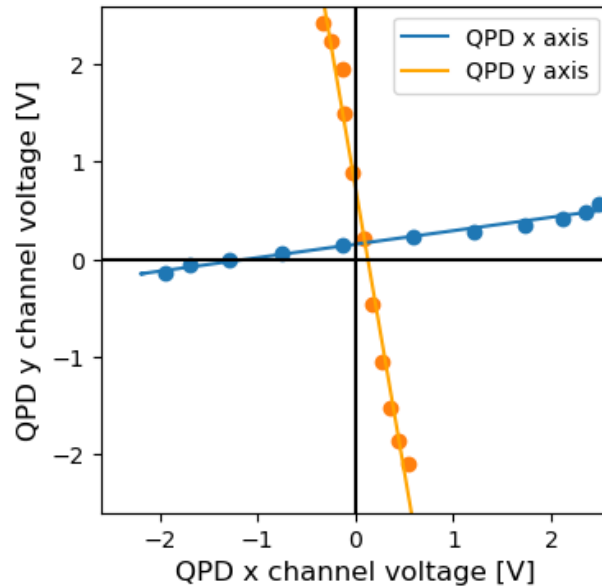


Figure 3.8: QPD Data fit showing rotation axis and center offset

To calibrate the QPD, we use a simple setup. We mount a fiber launch to a 2D translation stage, align the laser beam to the center of the QPD, and then use the 2D stage actuators to sweep the laser beam across the QPD's linear regime along the x and y axes independently. We get the data in fig. 3.7, which we can fit to obtain the rotation angle and the QPD response function.
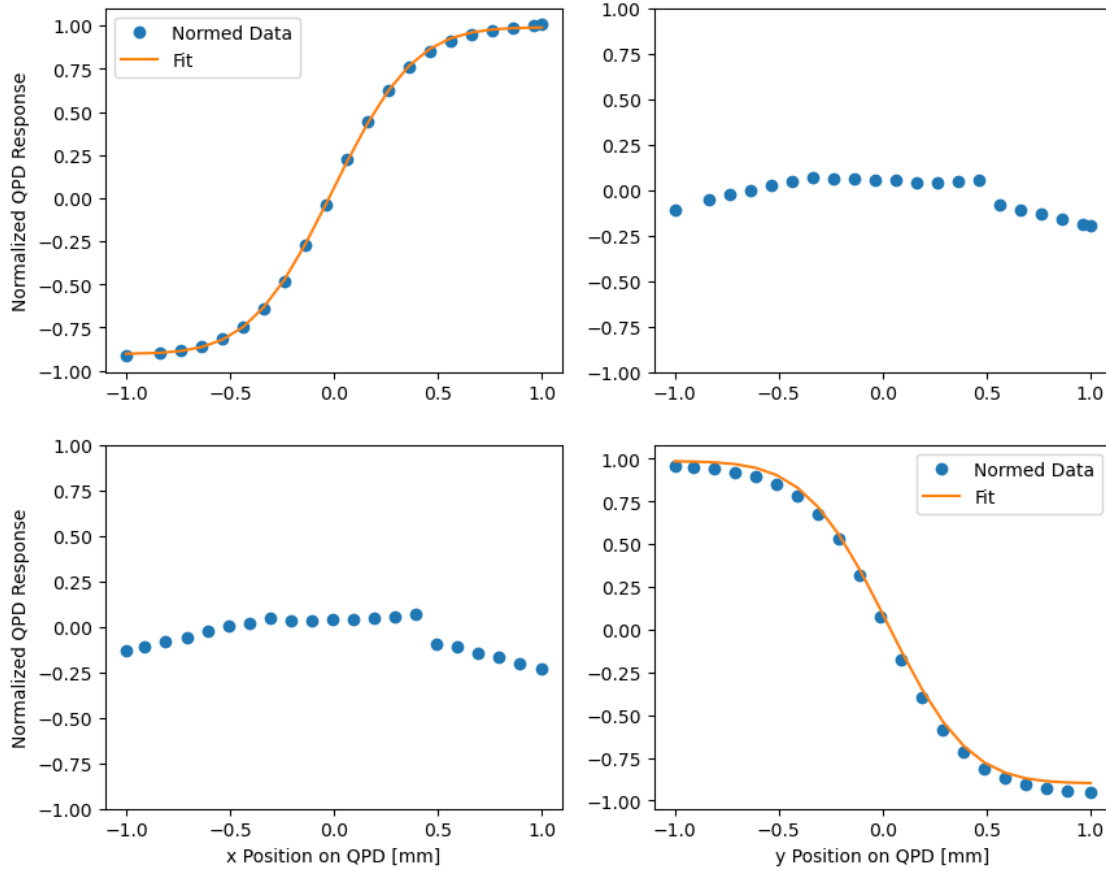
Figure 3.9: QPD Response as a Function of Position after Rotation

We begin by fitting for the rotation angle. We define the translation axes to be the standard x,y axes. To find the QPD axes, we plot the linear portion in fig. 3.7(a) against 3.7(b) and 3.7(c) against 3.7(d). This will result in the lines in fig. 3.8. We fit each line and get slopes m1, m2. Using these slopes, we compute the rotation angle as follows:

$$\theta_{\text{rot}} = \arctan\left(\frac{m_1 - m_x}{1 + m_1 m_x}\right).  \tag{3.9}$$

$m_1$ is the fitted x-slope in fig. 3.8 and $m_x$ is the slope of the x axis. We then rotate the data by the angle $\theta_{\text{rot}}$ using the 2D rotation matrix. This will ensure that moving along the x axis of the QPD will only couple into the x response of the QPD. Rotating the data in fig. 3.7 results in the data displayed in fig. 3.9. We see that off diagonal components are almost completely suppressed after rotation as expected. Using the calibration functions marked in orange in fig. 3.9, we can now convert measured voltages to positions. Since there is no analytical inverse to eq. 3.7, we must resort to numerical methods. We solve for the zeros of the following function:

$$R_{\text{QPD}}(x) - V_{\text{x}} = 0  \tag{3.10}$$

where $V_{\mathrm{x}}$ is the QPD response voltage and $R_{\mathrm{QPD}}(x)$ is the fitted QPD response function.

## 3.3   Piezo Characterization: Loaded Piezo

We present the results for the tests of the loaded piezo shown in fig. 3.3. Using a Michelson interferometer, we measure the stroke, linearity, and transfer function.

### 3.3.1   Piezo Stroke and Linearity Tests

After the Michelson is aligned, the camera is replaced with a photodetector and the detector is connected to a NIDaq card for data acquisition. Using a LabView program, a linear ramp is applied to the piezo. Since the piezo expands, one arm of the interferometer will change in length resulting in a differential phase between the two arms. The field in arm one is $\frac{E_0}{2}\exp i\omega t \exp 2ikl_1$ and the field in arm two is $\frac{E_0}{2}\exp i\omega t \exp 2ikl_2$. Here, $E_0$ is the incident field amplitude, $\omega$ is the frequency, $l_1$, $l_2$ are the optical path lengths for arm 1 and 2 respectively, and $k$ is the wavenumber. We hold arm 1 constant and change the length of arm 2 using the piezo. This means $l_2$ is a function of applied voltage. The total field after recombination is:

$$E_{\mathrm{tot}} = \frac{E_0}{2}e^{i\omega t}\left(e^{2ikl_1} + e^{2ikl_2}\right) \tag{3.11}$$

We care about the intensity of the electric field so we compute the magnitude of the field.

$$I = E_{\mathrm{tot}} * E_{\mathrm{tot}} = E_0^2 \cos^2\left(\frac{k\Delta l}{2}\right) \tag{3.12}$$

Here, $\Delta l = 2(l_1 - l_2)$. Since $k = 2\pi/\lambda$, constructive interference occurs $\Delta L = n\lambda$, and destructive interference occurs when $\Delta l = \frac{1}{2}(n+1)\lambda$ where n is a positive integer. To get a perfect reading of the stroke, we must read out the interferometer phase $\phi_{\mathrm{int}} = k\Delta l/2$. However, we get a good approximation by counting the number of interference fringes. The stroke is computed as

$$d = 2m\lambda \tag{3.13}$$

where $m$ is the number of interference fringes.

After applying a 140V linear ramp to the piezo and measuring the Michelson's response, we count 34 fringes as shown in fig. 3.10. Using eq. 3.13, we find the piezo's stroke to be $57.9 \pm .3$ $\mu$m. There are two reasons the piezo stroke is smaller than expected: first, we only apply a 140V ramp when the piezo is specified at 150V, and second the piezo is loaded by a small spring. Assuming the piezo response is linear in voltage, we expect the piezo to expand by $58.5 \pm 8$ $\mu$m at 140V. This is close to the measured value. Taking the small load into account, we find that load should reduce the stroke by about .05 $\mu$m according to eq. 2.5. This was computed by noting that the piezo has a stiffness of 26000 N/m, and the spring has a stiffness of 20 N/m. Ultimately, the values do agree.
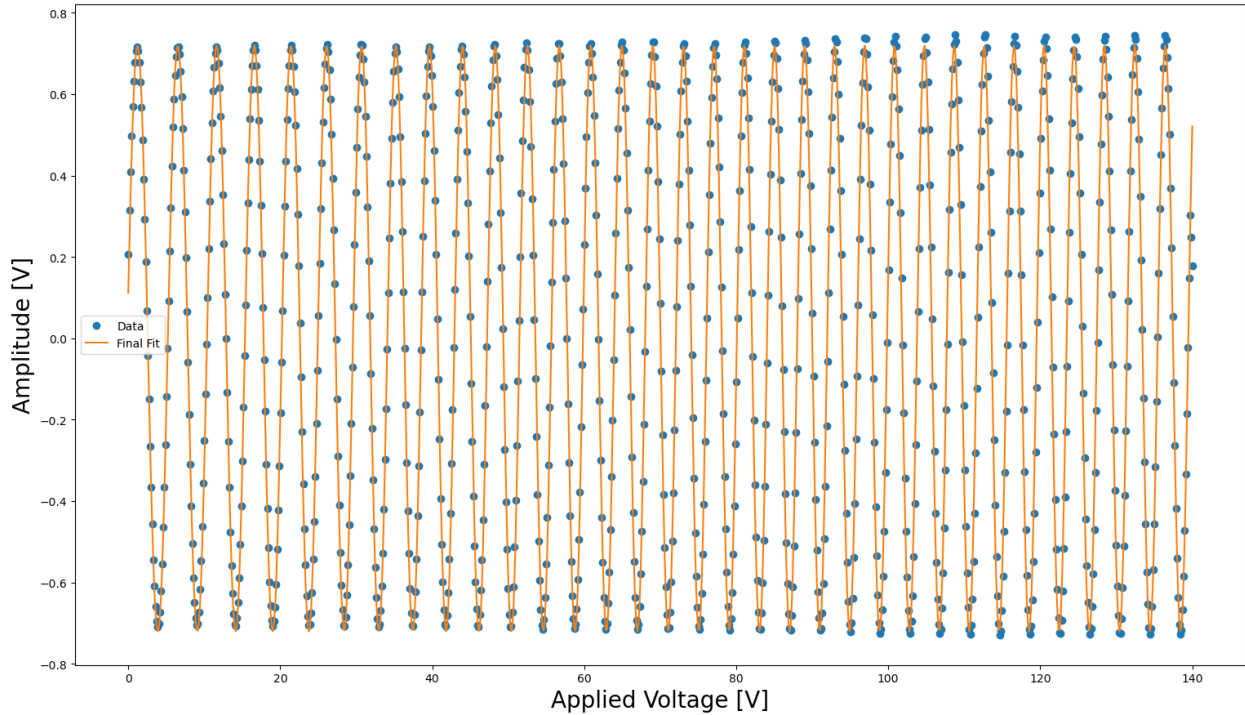
Figure 3.10: Michelson Response [V] vs Applied Voltage [v]

## 3.3.2 Piezo Transfer Function Measurement

To make the transfer function measurement, a LabVIEW program was written to control a signal generator, measure the photodetector output, and fit the photodetector output to a sine wave. By fitting the applied sine wave $S_1$ and the photodetector output $S_2$ to sine waves, we can measure the phase and gain of the piezo actuator. We have four fit parameters: $A_1$, $\phi_1$ and $A_2$, $\phi_2$. The gain is computed as:

$$G = \left| \frac{A_2}{A_1} \right| \tag{3.14}$$

and the phase is computed as:

$$\Delta\phi = \phi_2 - \phi_1 \tag{3.15}$$

We use the LabVIEW program to compute the two fits, the gain, and the phase. LabVIEW then plots the gain and phase as a function of applied frequency.

To get an accurate measurement, the measurement must start at a specific linear regime of a fringe. If you are on the positive slope, the interferometer moves closer to complete constructive interference if one arm is shortened, and the interferometer moves close to complete destructive interference if the arm is lengthened. The opposite occurs on the
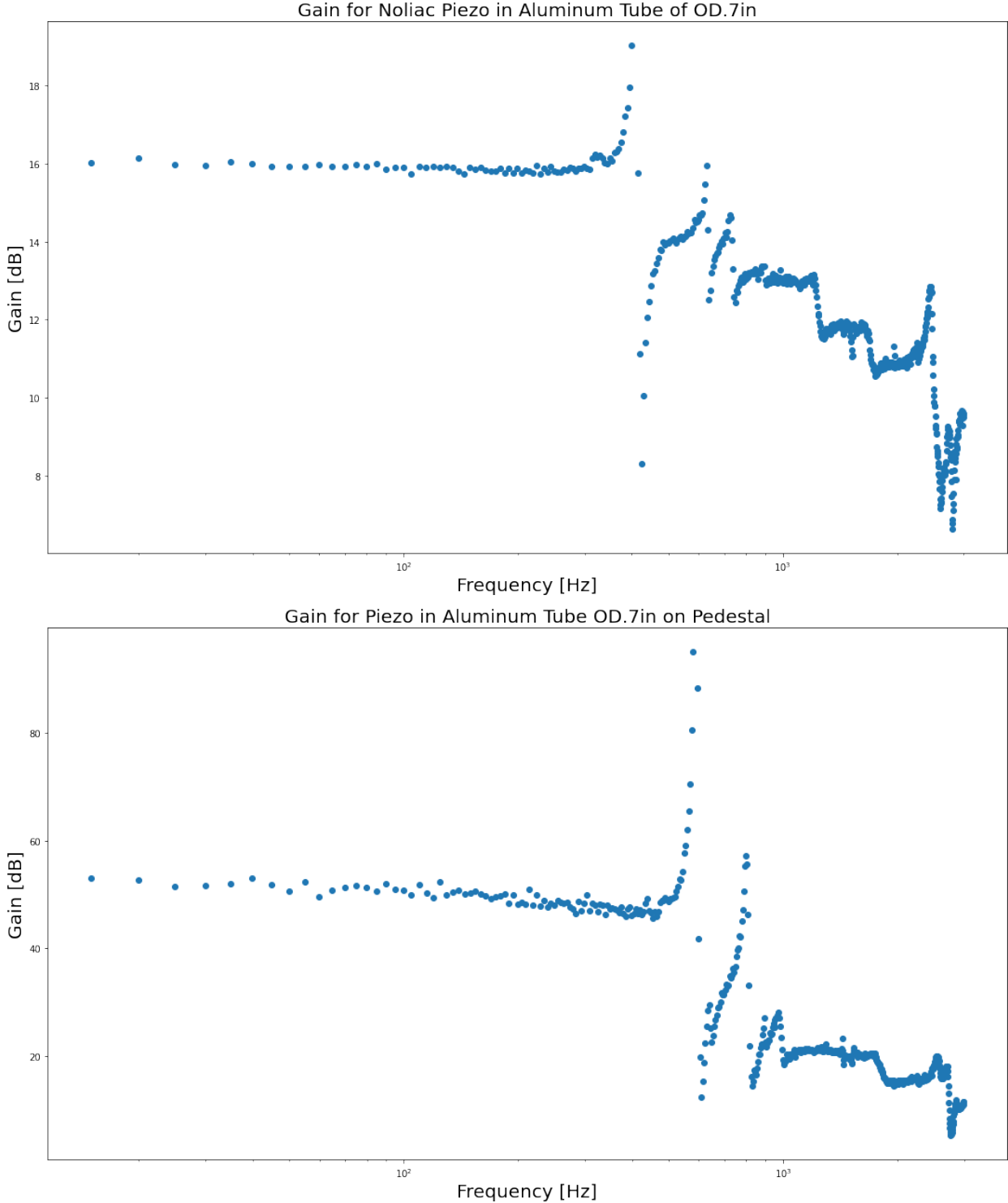
Figure 3.11: The gain response of the piezo in the aluminum mount. The top plot is for the aluminum piezo mount on a post while the bottom plot is for the aluminum piezo mount on a pedestal.

negative slope. To ensure this, we apply a small amplitude sine wave to the piezo and vary the DC offset until the splitting of the sine wave peaks are symmetric. To endure the Michelson stays in the linear regime during the measurement, all optics were mounted to pedestals and were as close to the optical table as possible; this provides about 30 minutes of stability, enough to make one transfer function measurement. We also observed that the piezo 'rings' when a voltage is first applied; that is, it rapidly drifts between interferometer fringes for about half an hour. We allow the piezo to settle mechanically before setting up the measurement.

We began by measuring the resonant frequency of the piezo on a Newport New Focus 9807 mount. The mirror mount was secured to the table using a 1.5" post and a 1.5" post holder. The piezo was about 3 inches above the surface of the optical table. Using the LabVIEW program, we applied a frequency sweep to the piezo from 1-10 kHz and noticed prominent sub-kHz resonances as shown in the top plot of fig. 3.11. However, the piezo specifications suggested the first piezo resonance might appear at frequencies > 10 kHz. We realized the mirror mount itself was resonating by feeling the entire mount vibrating.

To explore the piezo resonance onset, we began by placing a large mass ($\sim$ 100 g) on the rigidly mounted piezo and noticed the resonances dampened. We hypothesized that increasing the rigidity of the mount would reduce the mount's resonances. We secured the mirror mount to a short pedestal to a) increase the mass of the total structure and b) bring the mount as close to the optical table as possible. Rigidity should limit the motional modes of the mirror mount and damp high frequency vibrations. This pedestal scheme does indeed damp higher frequency resonances in the bottom plot fig. 3.11.

Two conclusions were drawn from the first resonance tests. The mass of the piezo mount and the mounting scheme determine the resonance behavior of the piezo mount. We decided to manufacture two additional tubes made out of stainless steel—one with the same outside diameter of .7in as the ThorLabs SM05L30 and the other with a larger outside diameter of .9in. This would change the mass and increase the rigidity of the mount. We tested each of the three tubes mounted on a post and a pedestal to see which combination resulted in the highest resonant frequency and most damped resonant features.

| Material | Outer Diameter [in] | Lowest Resonance on a Post [Hz] | Lowest Resonance on a Pedestal [Hz] |
|---|---|---|---|
| Aluminum | .7 | 399 | 579 |
| Stainless Steel | .7 | 359 | 469 |
| Stainless Steel | .9 | 289 | 434 |

Table 3.1: Resonant Frequencies for Different Mounting Schemes

As is shown in table 3.1, the pedestal performs better in every case, which is expected. However, it was unexpected that the heavier stainless steel tubes would have a lower resonant frequency than the aluminum tube.

We believe this could be explained by modelling the piezo mounts as simple harmonic oscillators. The resonant frequency of a harmonic oscillator with spring constant $k$ and mass

$m$ is given by:

$$\omega_0 = \sqrt{\frac{k}{m}}. \tag{3.16}$$

The resonant frequency is $\propto \sqrt{1/m}$ meaning that larger masses resonate as lower frequencies. We see that the resonant frequencies in table 3.1. decrease as roughly $1/\sqrt{m}$, consistent with our hypothesis.

A new way of clamping the piezo on the mirror mount with increased rigidity could therefore decrease the amplitude of sub-KHz resonances. To test this hypothesis, we manufactured a mount made from a steel block as see in fig. 3.12. It clamps onto the piezo tube as the mirror mount but is much simpler and bulkier.
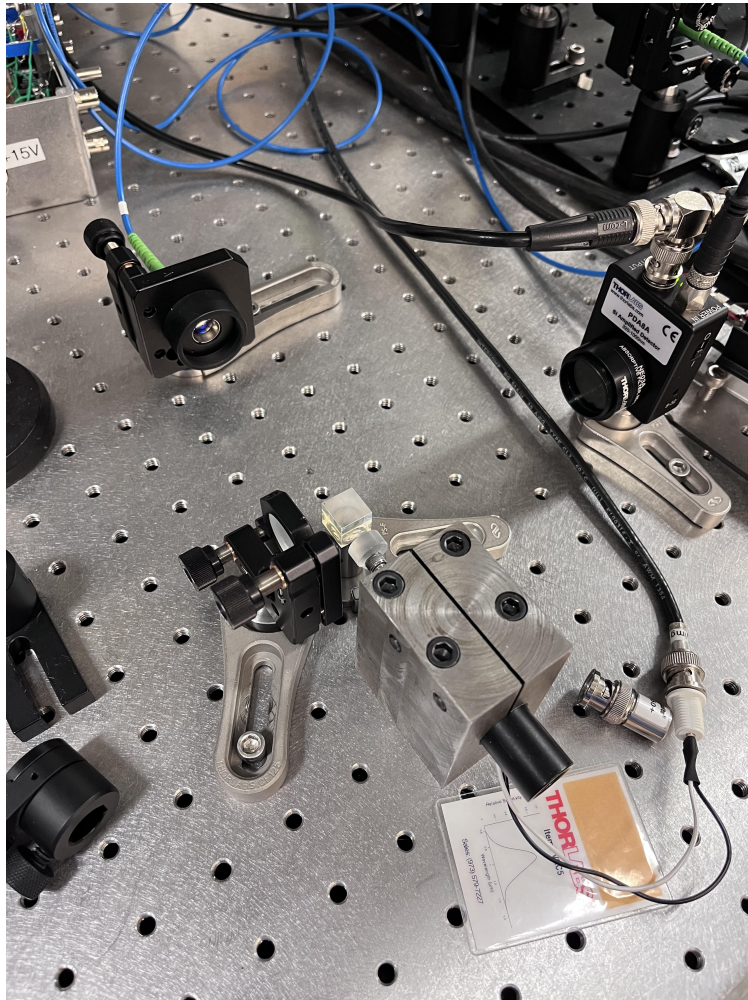


Figure 3.12: This mount is made from a large steel block. It was machined to clamp onto the tube using two 1/4-20 screws.
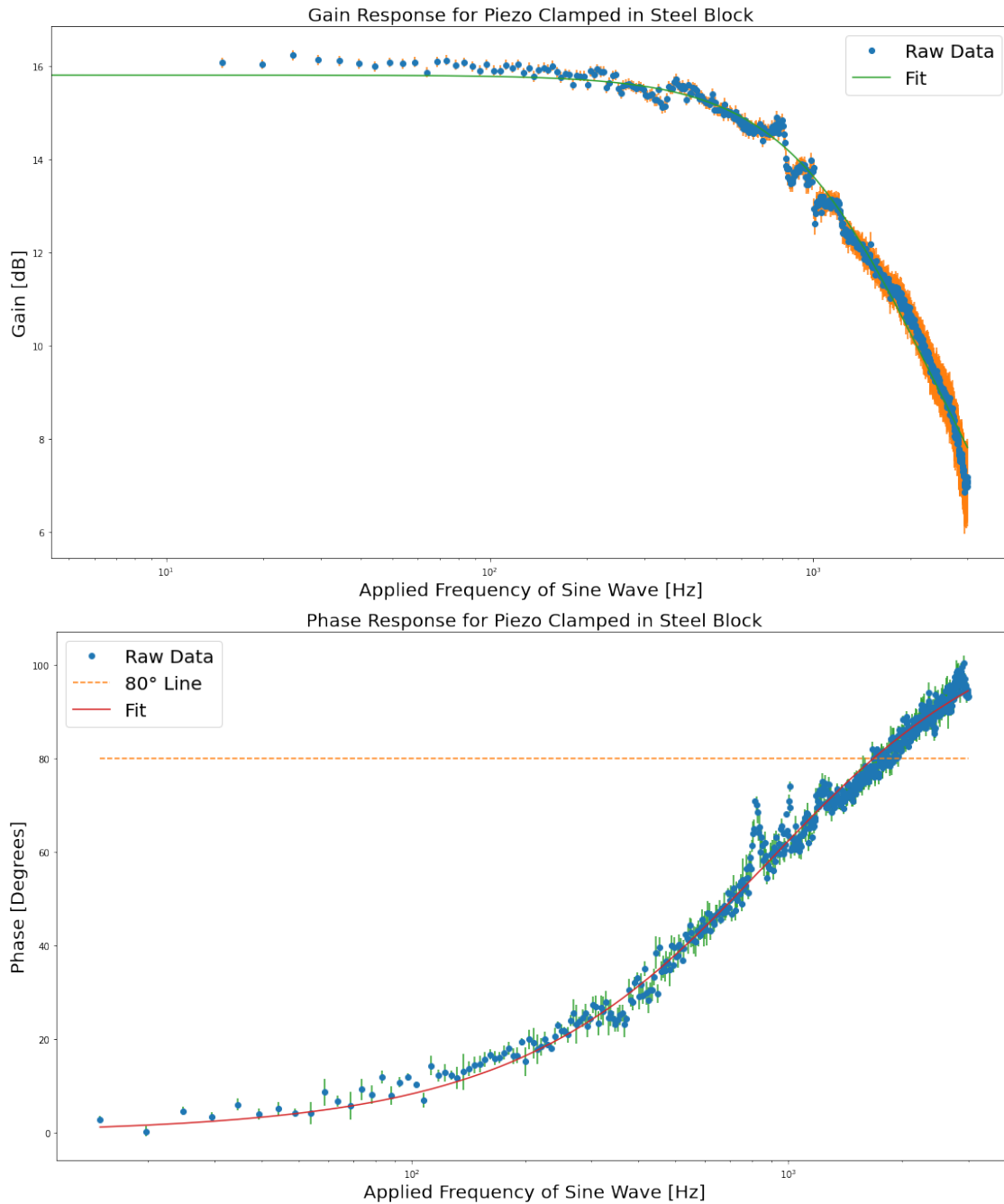
Figure 3.13: The transfer function for the large mass mount. The top graph is the gain as a function of frequency, and the bottom graph is the phase as a function of frequency. The fit models are given in eq. 2.9 and eq. 2.10.

The piezo actuator bandwidth in this configuration is not limited by the first resonance

anymore. We can now model the piezo's transfer function in the absence of resonances. The bandwidth of the feedback loop will be determined by the region where piezo gain is flat and phase delay is below 60 degrees [42]. We want to determine the piezo bandwidth using this criterion.

We expect the response to look like a low-pass filter with capacitance of 6500 nF and an unknown resistance as described in sec. 2.4.2. We fit the gain and phase to a passive low-pass filter. We can extract the resistance of the piezo from the fitted data. We see the fitted data in fig. 3.13.

We also see that fitting the data to a passive low-pass filter results in a good fit. This means that the bandwidth of this actuator is limited by the piezo's capacitance. Since the size of the piezo actuator determines the capacitance using a smaller piezo like the Noliac NAC2012-H30 should allow for higher bandwidths if needed. Ultimately, the bandwidth is limited by the piezo and mirror mount resonances. Through our investigations, we were able to increase the first resonant frequency by a factor of 10. Using these two methods, We would be able to actuate the piezo without worrying about mechanical resonances due to the mount or from phase shifts resulting in positive feedback.

## 3.4  Piezo Characterization: Piezo Screw

This section will discuss the performance of the piezo screw that will replace the slip-stick screw, as described in Section xyz. We first want to ensure that the piezo performs to the specifications provided by the manufacturer before completing more extensive tests to determine whether it meets the criteria discussed in sec. 2.1. We discuss measurements of the piezo stroke, linearity of response, and resonant frequency.

### 3.4.1  Measuring Piezo Stroke

We begin by describing how we use the QPD describe above in Section xyz to measure the stroke of the piezo. The piezo screw is mounted to a regular three-screw mirror mount. Actuating the piezo changes the laser's pointing. If we place a QPD 1 m away (fig. 3.14), we can measure this change in pointing, which we can convert to piezo displacement.

We use a LabVIEW program to generate a 7 V ramp which is later amplified by 26 dB of gain. This means we drive the piezo with 140 V ramp using a simple LabVIEW program. Using the same LabVIEW program, we read out $V_x$ and $V_y$ (eqs. 3.1a,3.1b) at every point along the 140 V ramp. This allows us to plot the normalized QPD response along each axis against the applied voltage.
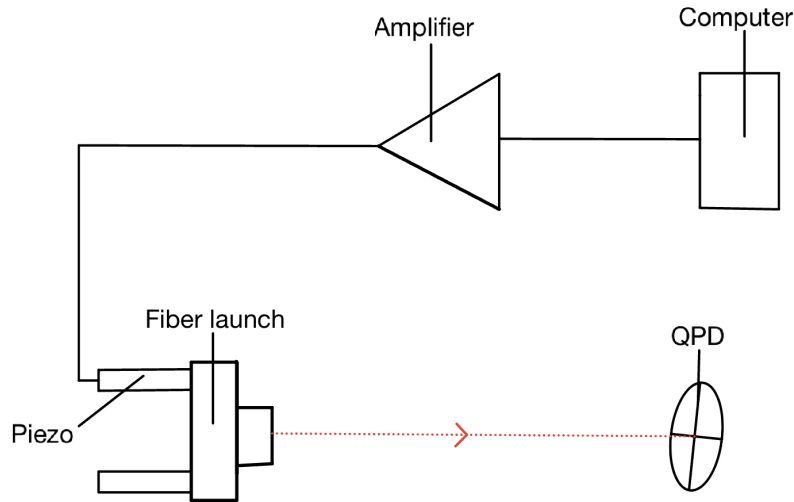
Figure 3.14: Piezo Screw Measurement Apparatus: Here the dashed red light is the laser and the solid black line is the BNC cable connecting the computer to the piezo.

To prepare the system for a measurement, we first align the laser to the center of the QPD. Since we expect the beam to move by $\sim 1.5$ mm, we move the beam about $\sim .75$ mm off center. This will ensure that the beam stays roughly in the linear regime of the QPD. When the system is aligned, we run the LabVIEW script.

After the first test, we first saw that the curve corresponding to the increasing ramp did not overlap with the curve corresponding to the decreasing ramp. That is, the piezo exhibited hysteresis. This is completely expected from piezos [33] so we continued taking data. What was more concerning was that the mirror mount appeared to drift over time as seen in fig. 3.15. These drifts are concerning since the piezo stacks only have a limited range. If the piezo screw is causing the mirror mount to drift significantly, this may cause the piezo to run out of range, preventing it from correcting for the thermal drifts. We must ensure that the piezo screws are causing very little (sub $\sim 20$ $\mu$rad).

Since we are using a custom micrometer screw, we needed to ensure that these drifts are not caused by the piezo screw moving. To test this, we first measured the drift of the fiber launch mount without the piezo screw in two different ways: using a camera and using the QPD. These showed that the fiber launch did not drift by more than a micron which is much too small to explain the observed drift.

We then decided to do a differential measurement. We split the fiber launch beam using a beamsplitter and set up a mirror to reflect the beam towards a camera; we replace one of the micrometer screws on the mirror mount (first a ThorLabs KM100T then a Newport low drift mount) with the piezo screw. Both beams are incident on a camera and are allowed to drift overnight. We then fit the beam positions in MATLAB and take the difference. The KM100T only drifted by 2 $\mu$rad while the Newport mount drifted by more than 400 $\mu$rad.

We then saw that the drift was correlated with the size of the voltage steps. When the voltage step was greater than 1 V, the drift was very large so we made the voltage steps .1 V. This helped increase the robustness of the measurements. Using small voltage steps of .1 V and increasing the time between steps lead acceptable levels of drift. After converting from voltage to position, we are left with the data in fig. 3.16.

We see that the total motion is 0.1655 mm. Since we place the QPD 0.25 m away from the fiber launch, we must back propagate to determine how much the piezo expands. After some trigonometry, we find that the piezo expands by $26 \pm 1$ $\mu$m. This is less that the $33 \pm 15\%$ specified by ThorLabs. This is because we only apply a 140 V signal instead of the 150 V specified by ThorLabs. This means we actually expect a stroke of about 30.8 $\mu$m $\pm$ 15%. In addition, the piezo is loaded by the two springs in the mirror mount. However, we do not know the spring constants for these springs so we can not quantitatively determine how much these springs will reduce the piezo stroke. Using an estimate of the spring constant, the stroke should diminish by about 1 $\mu$m. This means that we measure the stroke to be $25 \pm 2$ which agrees with 30.8 $\mu$m $\pm$ 15%.
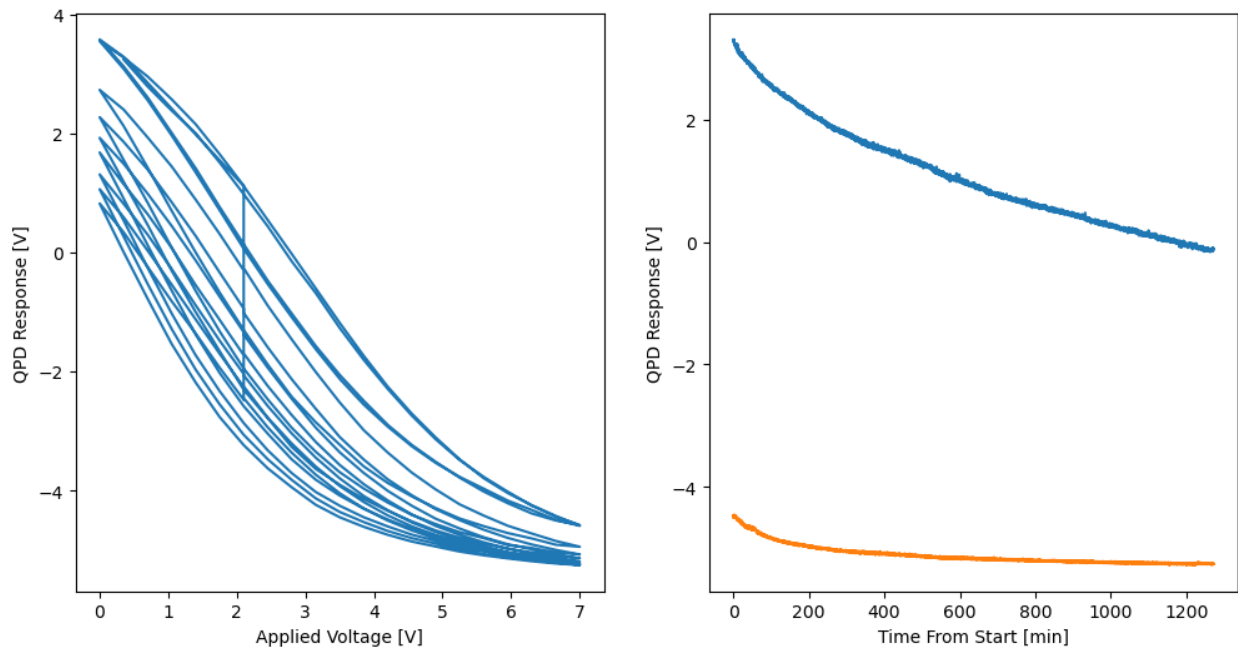


Figure 3.15: Drifting Stroke Measurement: Left: Hysteresis curve over 20 hrs; the curve drifts down over time. Right: Top and bottom turning points drift magnitude over 20 hrs.
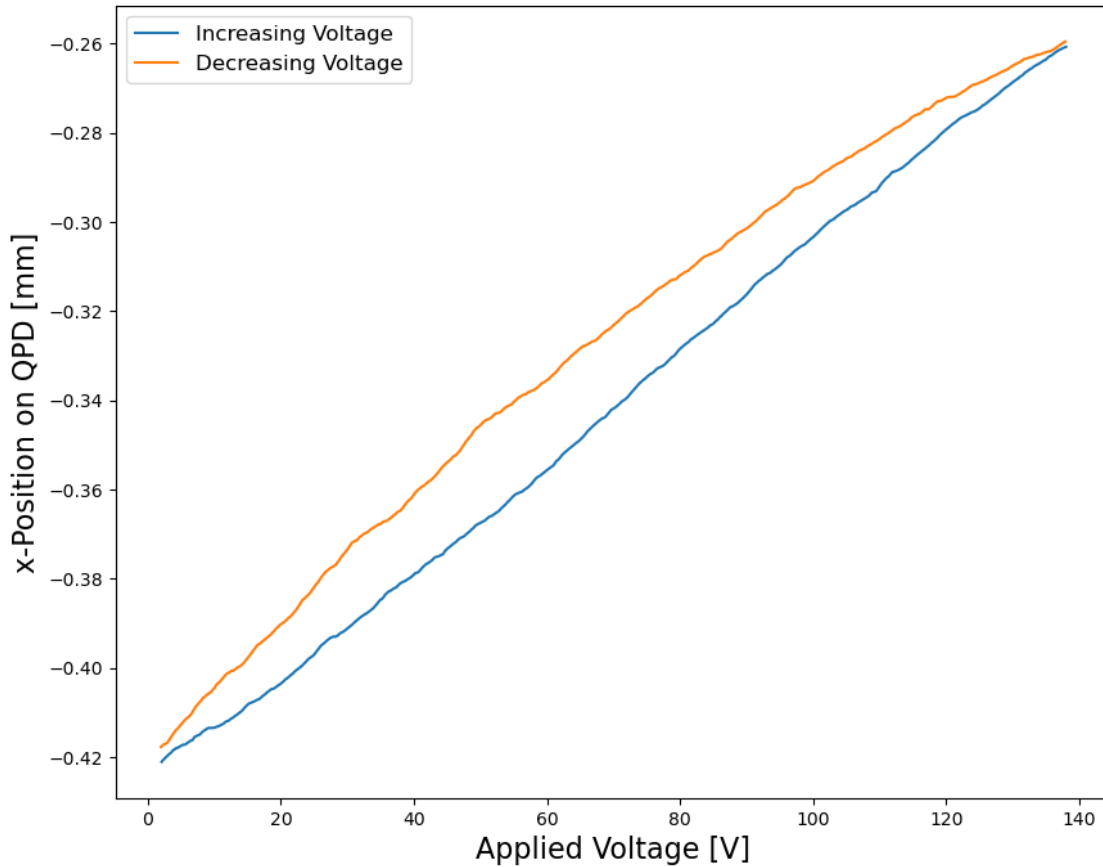
Figure 3.16: QPD x Position [mm] vs Applied Voltage [V]

## 3.4.2   Linearity of Piezo Response

We now want to determine the linearity of the piezo response. If the piezo response is non-linear, the gain of the feedback loops in sec 4.2 will change based on the voltage applied to the piezo. The linearity is thus extremely important to measure as it could cause the feedback loop to begin oscillating. However, since the systems are not currently built, it is difficult to conclude whether the observed variation in fig. 3.17 will negatively affect our feedback performance.

   To determine the gain of the piezo, we will take the derivative of the data in fig. 3.16. The derivative can be interpreted as the feedback gain as it has units of mm/V as shown in fig. 3.17. We see that the derivative varies by about a factor of 2. This means we may likely need to compensate for these changes in gain. Since the feedback loops are going to be implemented using a software LabVIEW integrator, this should be fairly easy to implement.
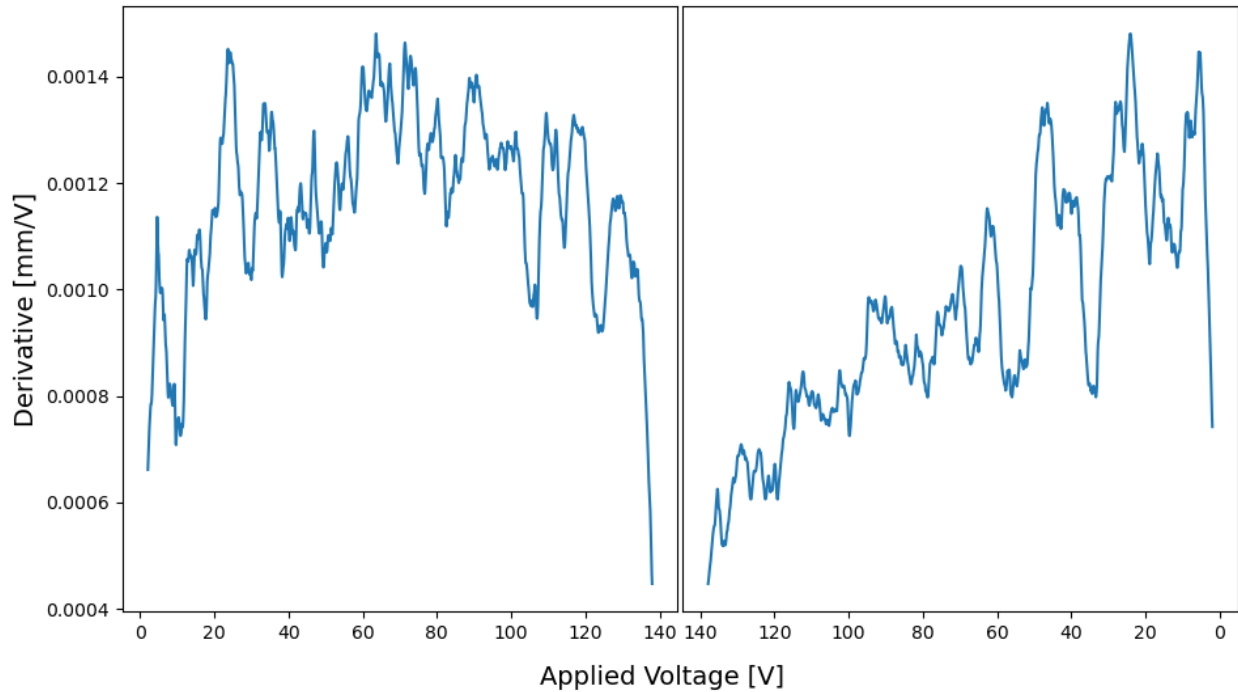
Figure 3.17: Derivative of data in fig. 3.16

### 3.4.3 Measuring the Mirror Mount's Transfer Function

This section is devoted to measuring the transfer function of the mirror mount. To measure the response, we will again use the QPD. We begin with the same setup in fig. 3.14. The only difference is the distance between the fiber launch and the QPD is reduced to 0.25 m. We use a LabVIEW program to control a Rigol signal generator. The signal generator outputs a pure sine wave of a specific frequency. This sine wave is amplified by the piezo amplifier with 26 dB of gain. The signal is then applied to the piezo and the response is measured with the QPD.

To ensure a proper measurement, we want the motion of the beam to stay in the linear regime of the QPD. Hitting a mirror mount resonance during the sweep would cause large motion of the mirror mount and cause the QPD to become misaligned. We thus want to apply a sine wave of small amplitude (0.1 V) to prevent measurement disruptions when crossing a mirror mount resonance.

We fit the QPD response to a sine wave and plot the gain and phase delay as a function of frequency. The results are plotted in fig. 3.18. We see that the first resonance occurs at 718 Hz which is well above the 100 Hz needed. Due to the complex resonant behavior, we cannot apply the simple filter model in sec. 3.3.2.
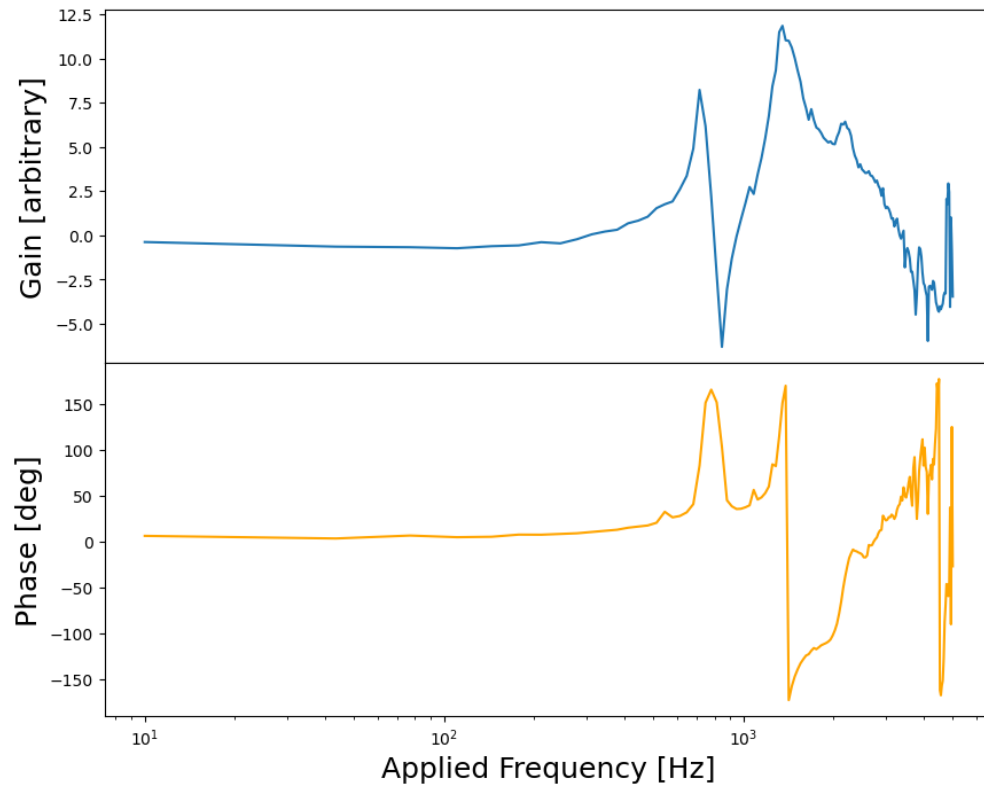
Figure 3.18: Mirror Mount Transfer function: The top plot is the gain and the bottom plot is the phase

Overall, the tests describe above show that piezo screw has range of $25\mu$m, are linear to a factor of 2, and bandwidth up to 718 Hz. These results match or surpass the requirements put forth in sec. 2.1. A future design will use a Noliac NAC2012 H30 piezo, which should increase the range around $35\mu$m. We find the slip-stick actuator suitable for replacing the micrometer screws in the Newport slip-stick piezo mount.

# Chapter 4

# Future Tests and Development

This chapter will provide an outline for the future testing and development of the mirror mount. Each section will describe a different step in the development process before installing the mirror mount in the vacuum chamber. In addition, some sections will provide detailed outlines for these tests and provide benchmarks for mirror mount performance. Section 1 will focus on vacuum compatibility of the full mirror mount. Section 2 will explore the Pound-Drever-Hall technique before showing the planned implementation of the two feedback systems: mirror steering and translation. Section 3 will discuss proposed tests for robustness; this will include longevity tests correlating laboratory conditions to the mirror mount performance. section 4 will summarize the work and present concluding remarks.

## 4.1 Vacuum Compatibility Tests

As mentioned in sec. 2.1.1, the mirror mount will be installed inside the vacuum chamber upon completion. The number of atoms remaining in the experiment is very sensitive to the pressures achieved inside the vacuum chamber [13]. Atom lifetimes, or the time before atom number decreases to $1/e$ of initial, in excess of 10s of seconds require pressures of $10^{-11}$ torr. To achieve these pressures, all components must be individually cleaned and tested. If any component outgasses above this level, careful analysis and redesigns will be required to limit outgassing as much as possible. This section will describe how to test components for vacuum compatibility.

### 4.1.1 Setting Up Test Vacuum

We use a separate, clean vacuum chamber dedicated for testing mirror mount components. This test chamber is comprised of a pumping stage, a vacuum chamber, and an residual gas analyzer (RGA) as shown in fig. 4.1. The pumping stage is attached to the vacuum chamber using a long, flexible bellow. The vacuum chamber must be large enough to fit the parts being tested and must also engage with the bellow. In this case, the chamber is a cube with

2.75" ConFlat (CF) flanges. Lastly, an RGA is attached directly to the chamber, so that the composition of the residual gas in the chamber can be sampled. The RGA must be operated above $\sim 10^{-8}$ torr and below 100 °C.
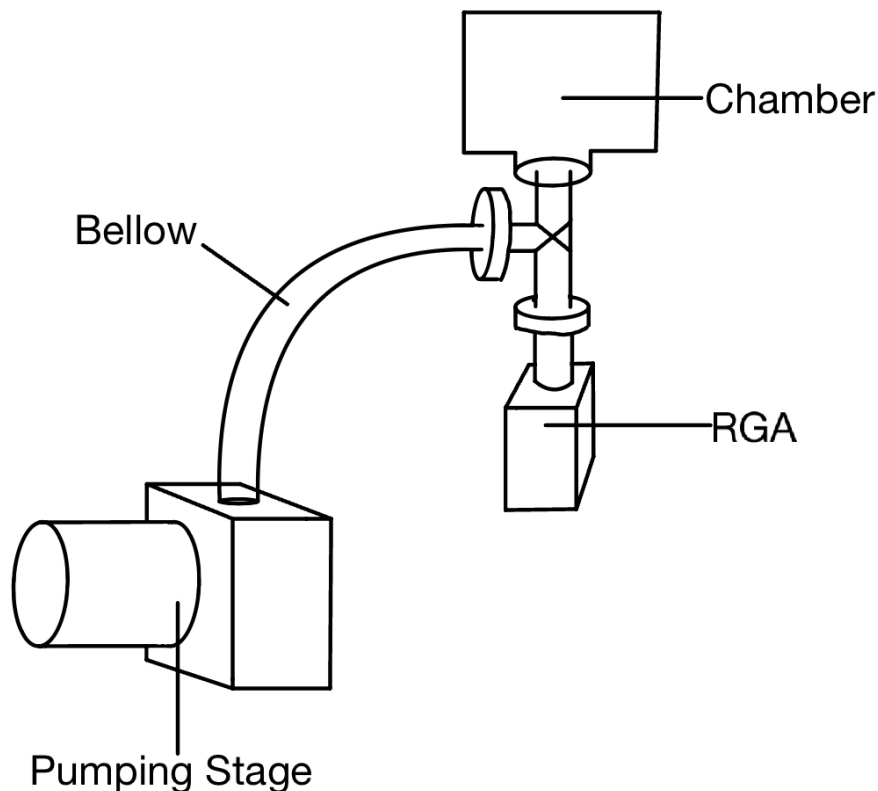


Figure 4.1: The test chamber as described in sec. 4.1. Test parts are loaded into the chamber.

Before testing the parts, they must be vacuum cleaned as follows. The parts are loaded into a large beaker for sonication. The first round of sonication uses a solution of detergent and water to remove as much dust and oil from the part. The parts should be sonicated for 30 minutes at 30 degC. After round 1, the parts are rinsed with water, returned to the beaker, and sonicated in acetone for 30 minutes at room temperature. The acetone is decanted into a waste container and the parts are sonicated in isopropanol for 25 minutes. If the parts contain materials sensitive to acetone such as some mirror coatings, skip the acetone step and use isopropanol directly. After the isopropanol, the parts are placed on UHV aluminum foil and allowed to air dry in a clean flow environment.

Once the three rounds are finished, the parts are considered vacuum cleaned so great care must be taken to prevent contamination. Gloves must be worn at all times when handling the parts. If the gloves become contaminated by touching an object that is not vacuum clean, they must be disposed of and replaced with new clean gloves. If the parts need to be stored, they must be wrapped in UHV aluminum foil. When assembling the vacuum

chamber, place UHV foil on the work surface, maintaining all clean parts on the foil. Place the parts in the chamber and carefully seal the vacuum chamber.

Once the chamber is sealed, the chamber must be "baked" to evaporate and pump away many of the contaminants. First, the chamber is wrapped in aluminum foil to improve thermal conductivity before carefully wrapping the chamber with heating strips. The heating strips should not overlap as this could create hotspots on the chamber and therefore damage the heating strips. Once the heating strips are placed correctly, another layer of aluminum foil should be wrapped to heat the chamber as uniformly as possible during "bake out".

After the heating strips are installed properly, the vacuum pumps are turned on and the chamber is allowed to pump down. At the same time, we begin to warm up the chamber for bake out. Since there are temperature sensitive components inside the chamber, we bake up to 100 °C for a week.

## 4.1.2 Vacuum Benchmarks
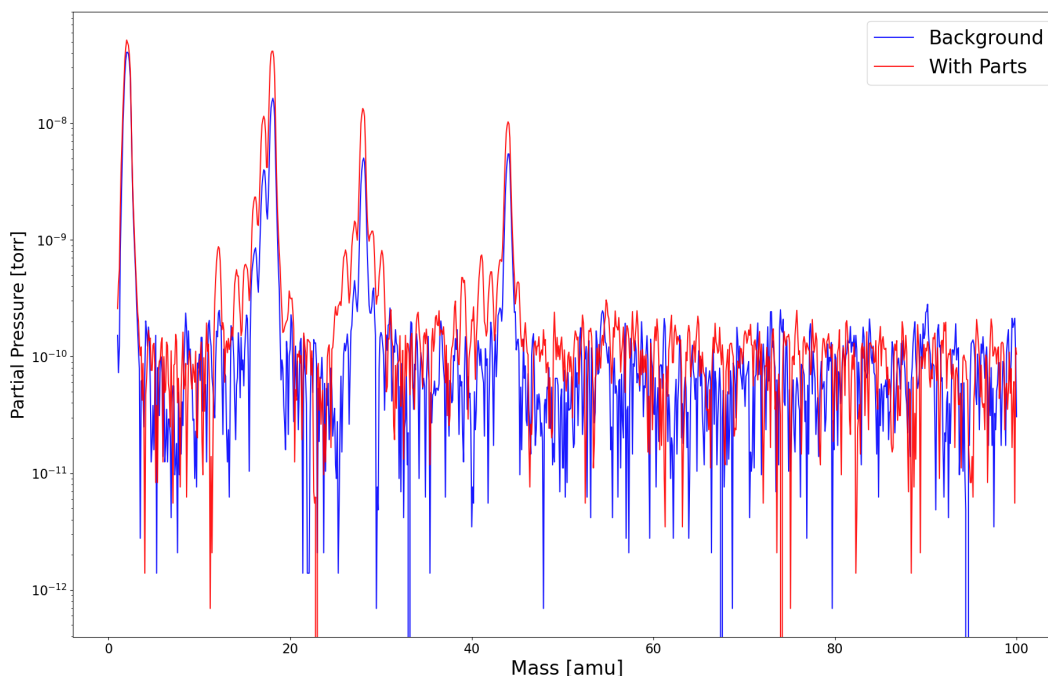


Figure 4.2: Partial Pressure [torr] vs Mass [amu] for the background and the parts

During the bake, we turn on the RGA to see the spectrum of gases present in the chamber. The RGA is essentially a mass spectrometer which measures the partial pressure of every gas. It plots the partial pressures against mass in AMU. After a week-long bake, we bring the vacuum down to room temperature again and take another RGA spectrum. We now turn to analyzing the RGA spectrums. There are two main comparisons to make. We first

want to compare the final RGA spectrum (S1) with the baked parts with an RGA spectrum of the empty chamber post bake (S2). If the peaks in S1 are much larger than the peaks in S2 (more than a factor of 10), there is an issue with the parts; check the parts for virtual leaks and ensure that all materials are vacuum compatible. If the difference in the size of the peaks is only about a factor of 3 or less like in fig. 4.2, then the parts have passed the first test.

After the first test, the RGA peaks are plotted as a function of the temperature during the bake out. We want to observe the peaks decreasing in size during the bake; if the peaks begin to increase at any point during the bake, we know that the parts are outgassing a compound with a mass corresponding to the peak of increasing size. If all the peaks are decreasing as in fig. 4.3, this confirms that the contaminants are being pumped out of the chamber by the "bake" process. Then the second test is met and the parts should be safe for use in the experiment chamber.
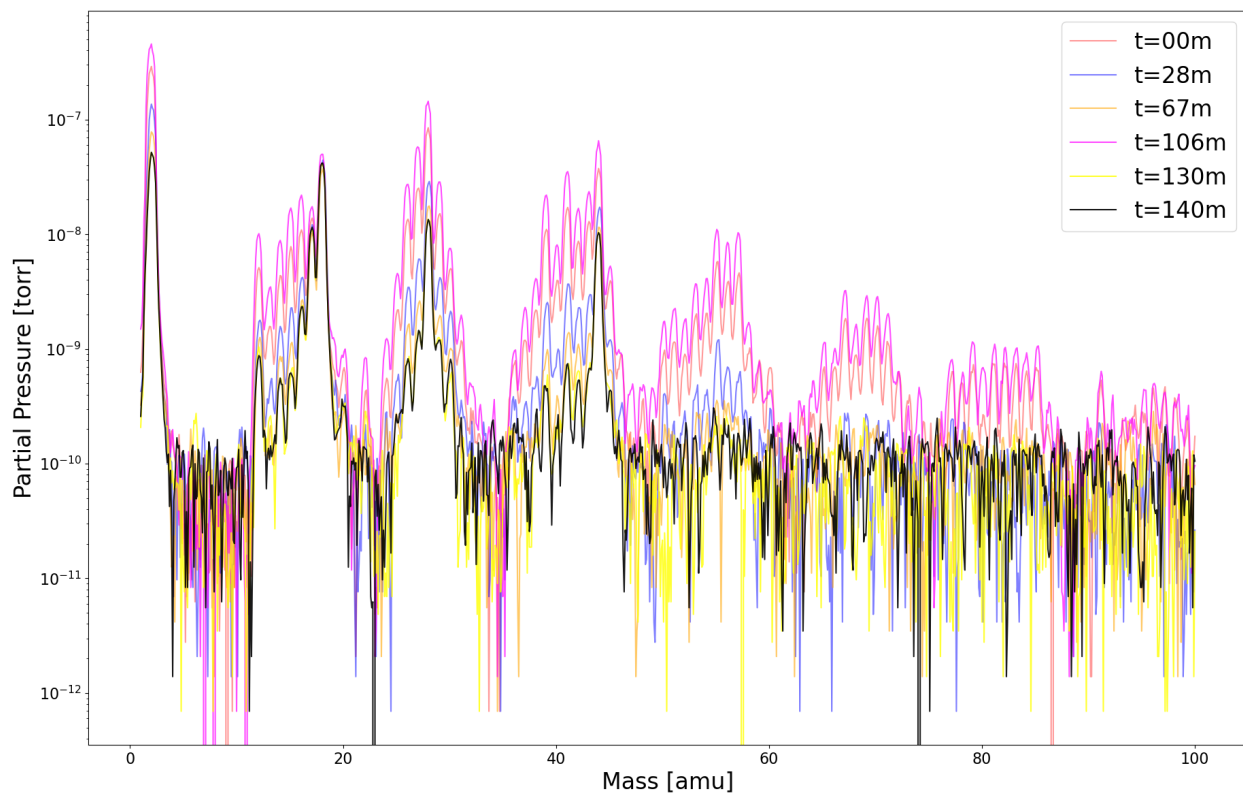


Figure 4.3: Partial Pressure [torr] vs Mass [amu] at different times during the bake

## 4.2   Cavity Feedback Systems

The primary goal of this project is to keep the cavity parameters (length, alignment, position) stable and well controlled as the experiment chamber drifts mechanically and thermally. Since we are attempting to control three degrees of freedom (cavity length, pointing in two axes), we require a feedback loop for each.

The first subsection will discuss the Pound-Drever-Hall (PDH) technique used to either lock a laser to a stable optical cavity or to lock a cavity to a stable frequency laser. We use PDH to generate the length corrections needed to keep the cavity's length as constant as possible. We will go through an intuitive derivation of the PDH signal before presenting the optical setup required for PDH. The second subsection will discuss using the QPD position measurements (sec. 3.2) to correct for the tip and tilt of the cavity mirror. This subsection will also show a diagram of what the complete feedback loop configuration should look like when implemented.

### 4.2.1   The Pound-Drever-Hall Technique:  Theory

The Pound-Drever-Hall Technique (PDH) is a process of generating an error signal which can be used to reference ("lock") a diode laser to a stable reference like high-finesse optical cavity or atomic transitions[25, 43]. This can correct for a diode laser's natural frequency drifts due to a variety of factors such as diode temperature and noise in the current supply. The laser can also be locked to a specific frequency determined by the optical cavity resonances [25].

We will not be using PDH to lock the laser to an optical cavity. Rather, we will lock our cavity to the laser. This allows for the precise control of the cavity length. In this section, we will discuss how PDH works theoretically by providing a brief derivation of the error signal.

Locking a laser's frequency is a simple idea which is non-trivial to implement [25]. Since we cannot directly measure the frequency of the laser on a photodetector since the laser frequency is to fast, we instead measure the frequency difference between the laser and the resonant frequency of a stable optical cavity, $\delta f$. The cavity length is set by a stable spacer with very good mechanical and thermal control. The idea is to dynamically adjust the laser's frequency to match the cavity's known and stable resonant frequency. To achieve this, it is required to continually measure the difference between the laser's frequency and the cavity's resonant frequency.

We can now use our knowledge of optical cavities to figure out how to accomplish the stated goal. Recall that light entering the cavity will only pass through if it is an integer multiple of $\Delta\nu_{FSR}$ [44]. This means when the laser frequency is far from a cavity resonance, all the light will be reflected, and if it is near resonance, more light will be transmitted through the cavity. We could use the reflected intensity of cavity to feedback on the laser, but there are two main issues with this method: first, it is dependent on the intensity of the laser which can fluctuate due to environmental factors, and more importantly, each reflection

Figure 4.4: Carrier and Sidebands: The effect of frequency modulating the laser with and RF signal. The blue signal is the transmission through the cavity, and the yellow signal is the reflection.

peak is symmetric about the minima meaning that we do not know which direction to tune the laser [25].

The PDH technique addresses the problems above by noting that the derivative of the reflection peaks with respect to $\delta f$ is anti-symmetric and will allow use to determine which way to tune the laser. The question now becomes how do we differentiate the reflected intensity. We accomplish this by modulating the frequency of the laser and observing how the reflected signal responds. After modulation, we will observe two sidebands (see fig. 4.4), one at higher frequency and one at lower frequency.

Near cavity resonance, the reflection of the carrier off the cavity will be phase shifted by $\pi$ rads with respect to the sidebands which are further away from the cavity resonance. The detector will show power at the modulation frequency with the laser frequency noise becoming sidebands centered around the modulation frequency. We finally mix this signal with the modulation signal as shown in fig. 4.6 and get a signal with odd symmetry which tells us how to correct the laser's frequency (see fig. 4.5)

The PDH lock, however, can only correct frequency changes within its "capture range". The capture range is basically the sideband frequency. This means if there is a cavity length change which is large compared to the capture range, the error signal won't know where the laser is and unlock.

We now turn to discussing how to generate the PDH error signal in the lab. We begin with a laser source (Newport Vantage TLB 7100 ECDL). The laser output for the typical external cavity diode laser (ECDL) laser is elongated in one direction so we need to shape the beam into something more manageable using an anamorphic prism pair(ideally, the Gaussian
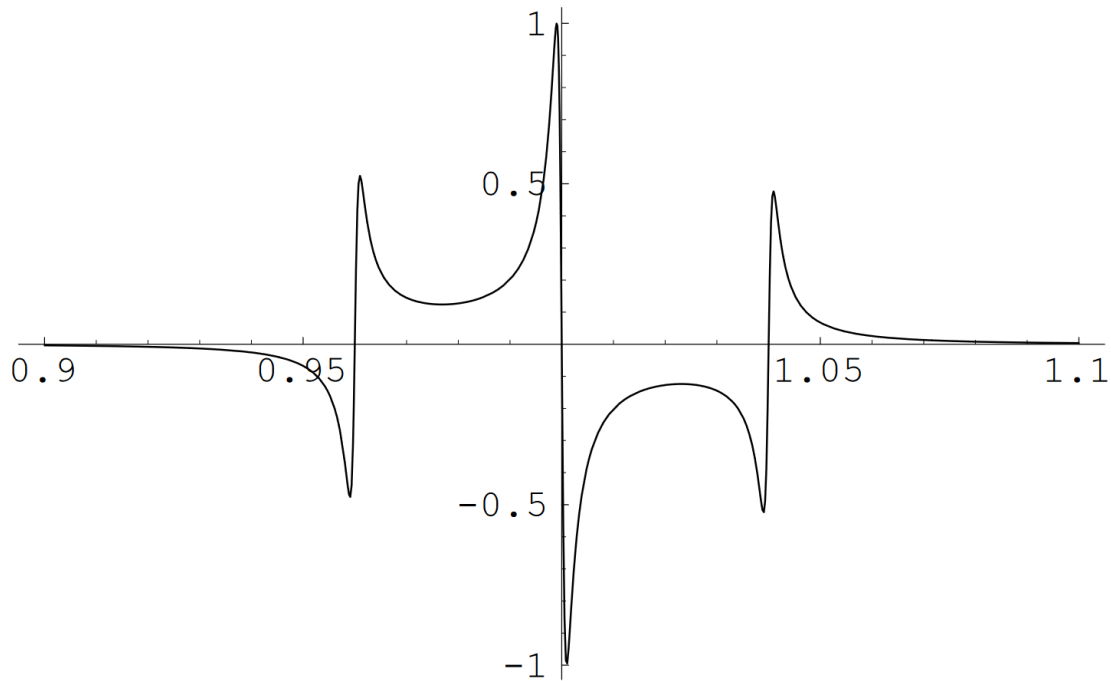
Figure 4.5: The PDH error signal as would be seen in the laboratory. Figure adapted from [45]

mode). Additionally, ECDLs are extremely sensitive to any sort of optical feedback so we need to make sure that no light is back-reflecting into the laser; to do this, we use an optical isolator which is a Faraday rotator with two polarizing beamsplitters at either end. The isolator has $-44$ dB of suppression; we require suppression below $-36$ dB.

The next part of the set up is where we phase modulate the laser. We use an Electro-Optical Modulator. EOMs need large amplitude RF signals to phase modulate the light, but most signal generators cannot provide such amplitudes. We use a simple LC tank circuit to resonantly enhance the RF signal at a modulation frequency of $\sim 10$ MHz. Additionally, we use a telescope to make sure the laser is focused enough to pass through the EOM crystal unclipped.

We then couple the light into an optical fiber due to its mode-filtering properties (ie. only the fundamental Gaussian mode passes). There is one potential drawback to using an optical fiber—if the polarization axis of the incoming light is not aligned with the fiber birefringence axis, the fiber will alter the polarization of the light which may cause intensity fluctuations if there is a polarizing, like a polarizing beamsplitter (PBS), downstream. We use a half-waveplate to match the polarization of the light with the polarization axis of the fiber.

The last section of the setup involves coupling into the optical cavity. We first need to

Figure 4.6: Optical setup for locking our ECDL laser. The dotted lines represent the laser beam and the solid lines represent coaxial cables.

determine how to separate the reflected beam from the incident beam on the cavity. The light entering the cavity is horizontally polarized. Using a PBS to separate the incident and reflected beams requires them to be orthogonal. Before entering the cavity, the incident beam passed through a quarter waveplate set at 45 deg; since the reflected beam passed through the quarter waveplate twice, the reflected beam can now be separated using the PBS. The reflected beam is readout using a fast photodetector. This signal is mixed with the EOM frequency before passing through a low-pass filter. The resulting signal is the PDH error signal. The PDH error signal passes through the proportional integration (PI) loop resulting in a correction

## 4.2.2   Stabilizing the Cavity Tilt

Similarly to the PDH error signal discussed in sec. 4.2, we use the QPD to generate an error signal for the position of the beam in the x and y direction by measuring the light in transmission (4.7). The error signal is also and odd function meaning that we can easily tell in what direction the mirror needs to move to correct for any tilts. The procedure for generating the error signal is outlined in sec. 4.2.1.

To correct for errors, each error signal is passed through a proportional integrator (PI) loop. After the correction is computed, the voltage is amplified by a high-voltage amplifier and fed to the correct piezo as shown in fig. 4.7.
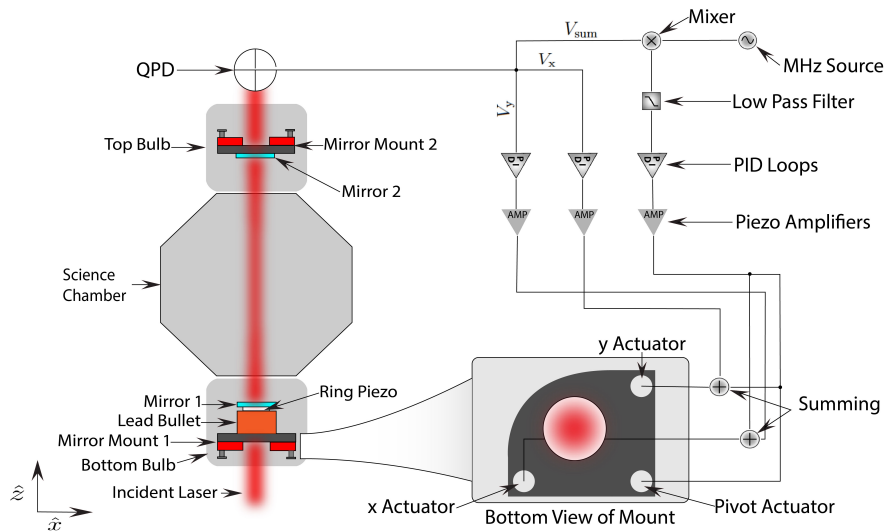


Figure 4.7: The science cavity with a diagram of the feedback systems. The cavity transmission is measured using the QPD. The QPD's four outputs are summed to become $V_x$, $V_y$, and $V_{\text{sum}}$ in software before being passed through a proportional integration (PI) loop. The output of the PI loops then amplified and passed to the piezos which correct the cavity length and alignment.

## 4.3    Robustness Tests

Before installing the mirror mount into the vacuum chamber, we must ensure that it is robust and performs adequately out of vacuum.  Once the mirror mount is installed in vacuum, it becomes extremely difficult to make modifications as breaking vacuum can put the experimental out of commission for several weeks if not longer. This section will outline some key tests to complete to ensure a robust mirror mount.

### 4.3.1    Testing for Mirror Mount Drifts

As discussed in sec 3.4.1, when testing a single piezo screw in a normal mirror mount, the mirror mount appeared to drift by as much as 100 $\mu$m. Since we were only using a single piezo screw, tests using all three should be conducted to guarantee that the mirror mount will not drift due to the piezo screws.
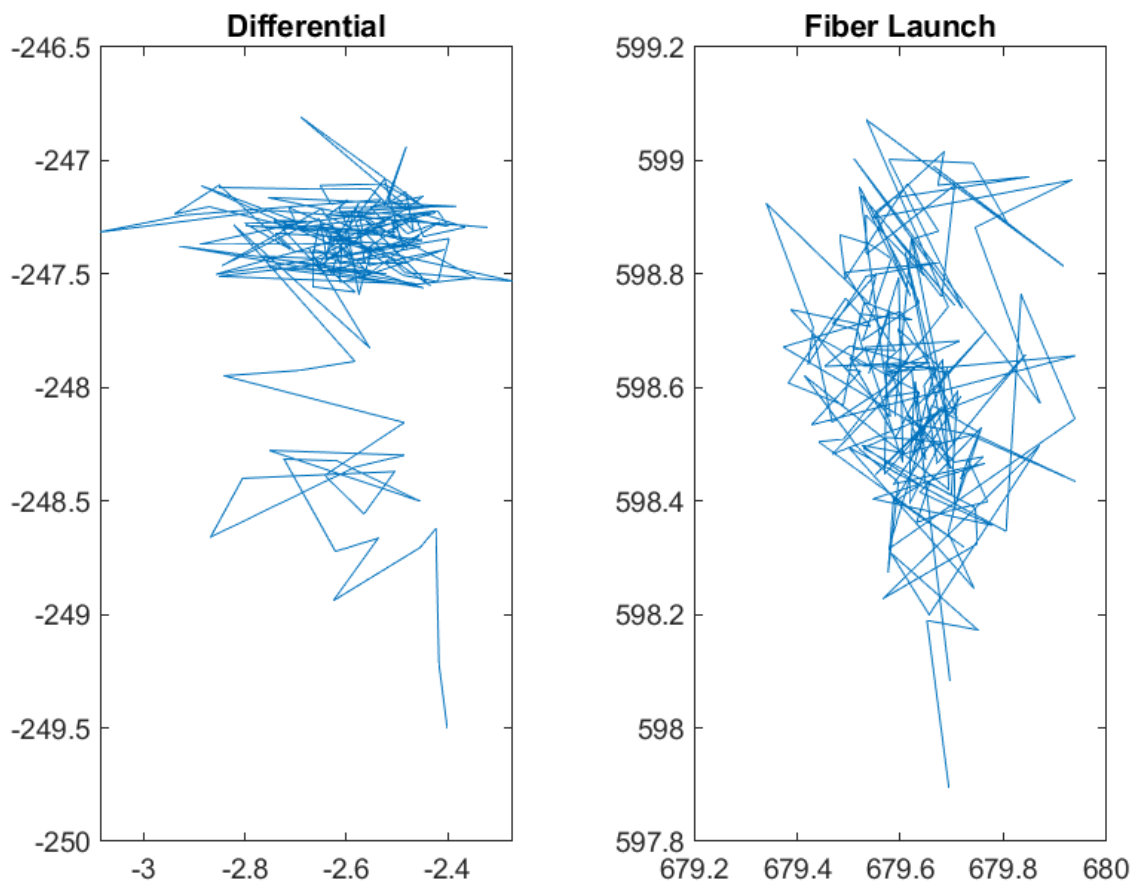
Figure 4.8: Mirror Mount Drift over 15 Hours: Each tick on the x and y axis represent one pixel. One pixel is 5.2 $\mu$m

There are a two tests to determine if the mirror mount will drift. The first is qualitative. When replacing the mirror mount's micrometer screws, we note how "tight" the thread feels when twisting the micrometer screw. Some resistance should be felt while unscrewing. If the same resistance is not felt while screwing in the piezo screw, this may indicate that the mirror mount will drift.

The second test involves measuring the motion of the mirror mount relative to a stable reference. To accomplish this, we follow the same procedure outlined in sec. 3.4.1. After allowing the camera to record the position of a laser reflected off the mirror mount, we can determine how much the reflected beam drifted relative to the reference. If the mirror mount drifts no more than one pixel (5.2 $\mu$m for our CMOS), then the mirror mount does not drift. In the test shown on fig. 4.8, the mirror mount mainly drifted in the y direction. Since the piezo screw controlled the x axis, the observed drift was unlikely to be caused by the piezo screw. This means the piezo screws are suitable for the mirror mount.

## 4.3.2   Testing Robustness of Feedback Systems

Before constructing the feedback systems and the full-scale test cavity, each individual actuator should be checked to ensure they all work. To test the actuators, mount a mirror to its surface and place the mirror mount on a pedestal. To measure the actuator response, reflect a laser off the mirror and into a camera as in fig. 4.9. Set the camera to be 50 cm away from the mirror mount. Connect each actuator to the proper piezo driver and scan over the actuator's full voltage range. The spot should move when scanning the tip, tilt actuators. Using the camera to measure the initial and final position of the actuator allows for a rough measurement of the actuator's stroke. This also shows that the piezo actuators and the slip-stick actuators are behaving as expected. If they are not, the cause should be investigated, determined, and fixed before further tests are conducted.

After the initial actuator tests are conducted, the full-scale test cavity and the feedback systems must be constructed as shown in fig. 4.7. The test cavity will be constructed outside of vacuum; this means ambient lab conditions will affect the cavity tremendously. A shield (for example a simple cardboard box) should be placed over the cavity to prevent air currents from disrupting the measurements. Once everything is ready, there are three things to complete: tune the feedback loops to lock the cavity, see whether the actuators can correct for the observed thermal drifts, and see how stable the lock is over long periods of time.

First, the PI loops must be tuned to lock the cavity. These loops are being implemented in software so the proportional and integral gain will be set using LabVIEW. Once the PI loops are properly tuned, the cavity will be locked. This can be seen by turning the PI loop on and off; when the PI loop is on, the error signal will integrate away and appear like a DC signal on an oscilloscope. While the PI loop is off, the PDH error signal will be present and look like fig. 4.5. In addition to tuning the PI loops, each piezo actuator will expand a different amount when a voltage is applied. To ensure that the three piezos expand uniformly to correct for the cavity length, the piezo response functions must be measured as

described in sec. 3.4.1. Then, choose the piezo with the smallest stroke and normalize each piezo response to this piezos.
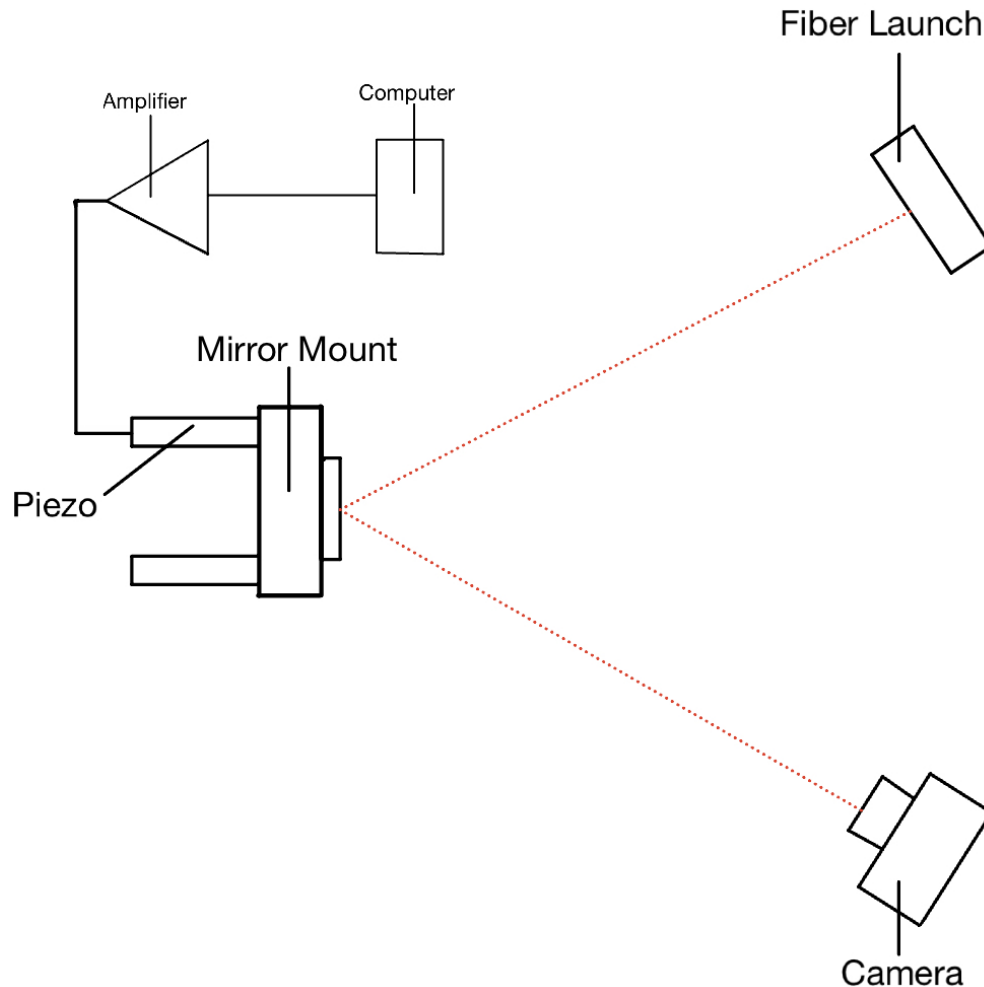


Figure 4.9: Test Setup for Rough Stroke Measurements

Once the feedback loops are tuned and the actuator gains are normalized, the feedback systems must be tested rigorously. Since the feedback systems are correcting for length and tilt drifts, we must apply noise to the system to see how the feedback systems perform. The cavity mirrors are separated by a metal spacer. If heating strips are placed on the spacer, we can measure how much the mirrors can drift apart before the cavity unlocks. The corrected drift must be greater than 26 FSRs as mentioned in sec. 2.1. Testing the cavity tilt control will be a bit more challenging. There are two ways to introduce tilts into the test cavity: using the micrometer screws on the top mirror mount or using the slip-stick actuators on the bottom mirror mount. Using the slip-sticks allows for precise control over the tilts applied.

When the cavity is locked, we will apply a known tilt using the slip-sticks. If the beam returns to the center of the QPD ($V_x = V_y = 0$ V), the system can correct for the applied tilt. Continue applying larger tilts until the beam does not return to the center of the QPD. If the feedback system can correct for tilts of $\sim 100$ $\mu$rad or greater, than the system should be able to control for the observed tilts in the science cavity.

Lastly, the feedback systems must be tested for long term stability. To test mirror mount robustness, we will lock the cavity and see how long it remains locked. At the same time, we will monitor the temperature inside the test cavity shield, the piezo applied voltage, and monitor the QPD $V_x$, $V_y$, and $V_{\text{sum}}$ for drifts. If any drift is correlated with the cavity unlocking, the drift should be investigated thoroughly and modifications to the mirror mount should be made. If the cavity stays locked for more than a week on several occasions while undergoing thermal cycles everyday, then the mirror mount can be installed in the chamber.

## 4.4 Conclusion

We have presented a design for a mirror mount using three large piezoelectric actuators to correct for thermal expansion of the cavity length and to suppress slow tilts. The devices capitalized on the piezo actuator's linear response to voltages, long stroke, and compact shape. The mirror mount will be able to correct for thermal drifts in the cavity length of at least 26 $\mu$m and correct for misalignment of the cavity axis with gravity of at least 100 $\mu$rad. The bandwidth will easily exceed the required 100 Hz. In addition, the piezo screw's compact design will result in minimal modifications to the in-vacuum optomechanics making installation easy. Through tests of the piezo screw detailed in sec. 4.3 and 4.4, we determine he prototype piezo screw has a stoke of 25 $\mu$m, a relatively linear response to applied voltages, and a resonate frequency of 718 Hz when engaged in a mirror mount. This means the design should work when assembled, allowing operation of the lattice interferometer for extended periods of time without drifts in the interferometer axis or cavity length.

# Bibliography

[1]   Thomas Young. "The Bakerian Lecture. Experiments and calculations relative to physical optics". In: *Philosophical Transactions of the Royal Society of London* 94.94 (1804), pp. 1–16.

[2]   R.W. Bunsen and G.R. Kirchoff. "Chemical Analysis by Spectrum Observations". In: *Philosophical Magazine* 4.20 (1860).

[3]   Max Planck. "On the Law of Distribution of Energy in the Normal Spectrum". In: *Annalen der Physik* 4 (1901), pp. 533–539.

[4]   Albert Einstein. "On a Heuristic Viewpoint Concerning the Production and Transformation of Light". In: *Annalen der Physik* 17 (1905), pp. 132–148. DOI: `https://doi.org/10.1002/andp.19053220607`.

[5]   Louis de Broglie. "A Tentative Theory of Light Quanta". In: *Philosophical Magazine* 6.47 (1824), pp. 446–458. DOI: `https://doi.org/10.1080/14786442408634378`.

[6]   Clinton J. Davisson and Lester H. Germer. "Reflection of Electrons by a Crystal of Nickel". In: *Proceedings of the National Academy of Sciences* 14 (1928), pp. 317–322.

[7]   Uwe Sterr, Laus Sengstock, Wolfgang Ertmer, Fritz Riehle, Jurgen Helmcke. *Atom Interferometry*. Academic Press, 1996.

[8]   Tycho Sleator, Oliver Carnal, Tilman Pfau, Andreas Faulstich, Hiroshi Takuma, Jurgen Mlynek. "Atom interferometry with mechanical structures". In: *World Scientific* (1992), pp. 264–271.

[9]   Mark Kasevich and Steven Chu. "Atomic interferometry using stimulated Raman transitions". In: *Physical Review Letters* 67.181 (1991). DOI: `https://doi.org/10.1103/PhysRevLett.67.181`.

[10]  Victoria Xu. "Lattice Atom Interferometry in an Optical Cavity". PhD thesis. University of California, Berkeley, 2020.

[11]  Zachary Pagel, Weicheng Zhong, Richard H. Parker, Christopher T. Olund, Norman Y. Yao, and Holger Müller. "Symmetric Bloch oscillations of matter waves". In: *Physical Review A* 102.053312 (2020). DOI: `10.1103/PhysRevA.102.053312`.

[12]  David M. Giltner, Roger W. McGowan, and Siu Au Lee. "Atom Interferometer Based on Bragg Scattering from Standing Light Waves". In: *Physical Review Letter* 75.2638 (1995). DOI: https://doi.org/10.1103/PhysRevLett.75.2638.

[13]  Cristian D. Panda, Matt Tao, James Egelhoff, Miguel Ceja, Victoria Xu, and Holger Müller. "Minute-scale gravimetry using a coherent atomic spatial superposition". In: *arXiv* (2023). DOI: https://arxiv.org/abs/2210.07289.

[14]  Achim Peters, Keng Yeow Chung, and Steven Chu. "Measurement of gravitational acceleration by dropping atoms". In: *Nature* 400 (1999), pp. 849–852. DOI: DOI:10.1038/23655.

[15]  Richard H. Parker, Chenghui Yu, Weicheng Zhong, Brian Estey, and Holger Müller. "Measurement of the fine-structure constant as a test of the Standard Model". In: *Science* 360 (2018), pp. 191–195. DOI: 10.1126/science.aap7706.

[16]  Marcus Arndt. "Free-Falling Interferometry". In: *Physics* 6.23 (2013).

[17]  Paul Hamilton, Matte Jaffe, Philipp Haslinger, Quinn Simmons, Holger Müller, and Justin Khoury. "Atom-Interferometry Constraints on Dark Energy". In: *Science* 349.6350 (2015), pp. 849–851. DOI: 10.1126/science.aaa8883.

[18]  E. L. Raab, M. Prentiss, Alex Cable, Steven Chu, and D. E. Pritchard. "Trapping of neutral sodium atoms with radiation pressure ". In: *Physical Review Letters* 59.263 (1987). DOI: https://doi.org/10.1103/PhysRevLett.59.2631.

[19]  Paul D. Lett, Richard N. Watts, Christoph I. Westbrook, William D. Phillips, Phillip L. Gould, and Harold J. Metcalf. "Observation of Atoms Laser Cooled below the Doppler Limit". In: *Physical Review Letters* 61.169 (1988). DOI: https://doi.org/10.1103/PhysRevLett.61.169.

[20]  Mahiro Abe et. al. "Matter-wave Atomic Gradiometer Interferometric Sensor (MAGIS-100)". In: *Quantum Science and Technology* 6.044003 (2021). DOI: 10.1088/2058-9565/abf719.

[21]  Manuel Andia, Raphaël Jannin, François Nez, François Biraben, Saïda Guellati-Khélifa, and Pierre Cladé. "Compact atomic gravimeter based on a pulsed and accelerated optical lattice". In: *Physical Review A* 88.031605(R) (2013). DOI: https://doi.org/10.1103/PhysRevA.88.031605.

[22]  Victoria Xu, Matt Jaffe, Cristian D. Panda, Sofus L. Kristensen, Logan W. Clark, and Holger Müller. "Probing gravity by holding atoms for 20 seconds". In: *Science* 366.6466 (2019), pp. 745–749. DOI: 10.1126/science.aay6428.

[23]  Anthony E. Siegman. *Lasers.* Sausalito: University Science Books, 1986.

[24]  Matt Jaffe. "Atom interferometry in an optical cavity". PhD thesis. University of California, Berkeley, 2018.

[25] Richard W. Fox, Chris W. Oates, Leo W. Hollberg. "Stabilizing diode lasers to high-finesse cavities". In: *Experimental Methods in the Physical Sciences* 40 (2003), pp. 1–46. DOI: `https://doi.org/10.101/S1079-4042(03)80017-6`.

[26] Travis C. Briles, Dylan C. Yost, Arman Cingöz, Jun Ye, and Thomas R. Schibli. "Simple piezoelectric-actuated mirror with 180 kHz servo bandwidth". In: *Optics Express* 18.10 (2010), pp. 9739–9746. DOI: `https://doi.org/10.1364/OE.18.009739`.

[27] *Piezo Motion Control Tutorial - Piezo Basics for Precision Motion, Force Generation Nanopositioning Applications in Industry and Research*. Physik Instrumente.

[28] *Voice Coils*. Industrial Quick Search.

[29] *Piezoelectric Inertia Actuators*. 2022.

[30] E. Magnan, J. Maslek, C. Bracamontes, A. Restelli , T. Boulier, and J. V. Porto. "A Low-Steering Piezo-Driven Mirror". In: *Review of Scientific Instruments* 89.7 (2018). DOI: `https://doi.org/10.1063/1.5035326`.

[31] S. C. Minne, S. R. Manalis, and C. F. Quate. "Parallel atomic force microscopy using cantilevers with integrated piezoresistive sensors and integrated piezoelectric actuators". In: *Applied Physics Letters* 67.26 (1995), pp. 3918–3920. DOI: `https://doi.org/10.1063/1.115317`.

[32] Víctor Ruiz-Díez, Jorge Hernando-García, Javier Toledo, Abdallah Ababneh, Helmut Seidel, and José Luis Sánchez-Rojas. "Piezoelectric MEMS Linear Motor for Nanopositioning Applications ". In: *Actuators* 10.2 (2021). DOI: `https://doi.org/10.3390/act10020036`.

[33] Ravinder S. Dahiya and Maurizio Valle. *Robotic Tactile Sensing: Technologies and System*. Hanover: Springer, 2013.

[34] *IEEE Standard on Piezoelectricity*. 1988.

[35] *Piezoelctric Basic Background and Operation Tutorial*. 2019.

[36] Jina Kim, Benjamin L. Grisso, Jeong K. Kim, Dong Sam Ha, and Daniel J. Inman. "Electrical Modeling of Piezoelectric Ceramics for Analysis and Evaluation of Sensory Systems". In: *IEEE Xplore* (2008). DOI: `10.1109/SAS13374.2008.4472956`.

[37] Derek Rowell. "Impedance-Based Modeling Methods". 2003.

[38] Marc Rioux and Jacques Domey. "Lateral effect photodiode: a new technique to obtain position signals". In: *Applied Optics* 21.20 (1982). DOI: `https://doi.org/10.1364/AO.21.003618`.

[39] *PSD Characteristics*. Osi Optoelectronics.

[40] A. Vera-Marquina, A. Diaz Sanchez, J. Miguel Rocha-Pérez, D. Berman-Mendozaa, Ivan Padilla. "Quadrant photodiode for electronic processing". In: *Proceedings of SPIE - The International Society for Optical Engineering* 7419 (2009). DOI: `https://doi.org/10.1117/12.825520`.

[41]   Jadze Narag and Nathaniel Hermosa. "Response of quadrant detectors to structured beams via convolution integrals". In: *Journal of the Optical Society of America A* 34.7 (2017), pp. 1212–1216. DOI: https://doi.org/10.1364/JOSAA.34.001212.

[42]   Weng Khuen Ho, Change Chieh Hang, and Lisheng S. Chao. "Tuning of PID controllers based on gain and phase margin specifications". In: *Automatica* 31.3 (1995), pp. 497–502. DOI: https://doi.org/10.1016/0005-1098(94)00130-B.

[43]   Wojciech Gawlik and Jerzy Zachorowski. "Stabilization of diode-laser frequency to atomic transitions". In: *Optica Applicata* 34.4 (2004).

[44]   Norman Hodgson and Horst Weber. *Laser Resonators and Beam Propagation Fundamentals, Advanced Concepts, Applications.* Springer, 2005, pp. 189–217.

[45]   Eric Black. "Notes on the Pound-Drever-Hall technique". Apr. 1998.